Effect of Interplanetary Shock Impact Angle on the Occurrence Rate and Properties of Pc5 Waves Observed by High-Latitude Ground Magnetometers

Andrew Ballard Baker

Thesis submitted to the faculty of the Virginia Polytechnic Institute and State University
in partial fulfillment of the requirements for the degree of

Master of Science
In
Electrical Engineering

Robert C. Clauer
Michael D. Hartinger
Scott M. Bailey

April 19, 2019
Blacksburg, VA

Keywords: Interplanetary Shocks, Ultra Low Frequency Waves, Pc5 Waves

Effect of Interplanetary Shock Impact Angle on the Occurrence Rate and Properties of Pc5 Waves Observed by High-Latitude Ground Magnetometers

Andrew Ballard Baker

ABSTRACT

The effects of interplanetary shock impact angles have the potential to have far reaching consequences. By their nature, interplanetary shocks are a direct consequence of a variety of solar events including both Coronal Mass Ejections (CMEs) and Co-rotating Interaction Regions (CIRs). They have the ability to move the magnetopause, the boundary between the Earth's magnetosphere and the surrounding plasma, leading to ionospheric current systems and an enhanced ring current. Their association with a time-varying EMF also makes them potentially dangerous at a human level. This EMF can couple to electrical currents in technological infrastructure that can overload transformers, communication cables, and power grids. As IP shocks have the potential to have a large impact on our society, research to further our understanding of these events is prudent. We know that shocks can couple to currents and ULF waves in the magnetosphere-ionosphere system. Much of the current research into their behaviors has been focused on models and simulations and has indicated that the shock impact angle should affect the properties of the waves. To investigate the potential influence of the impact angle, data from a series of Antarctic magnetometers was collected and compared to a database of known interplanetary shocks to determine when the response to different shocks was detected at the magnetometer. For this investigation, we were concerned with determining what impact if any, the impact angle of the IP shock had on the generation of Pc5 waves. To that end, the power spectra both before and after the shock was calculated. This information was then combined with the shock impact angle to determine what effects if any, the shock impact angle had on Pc5 wave occurrence rates. From our research, it was determined that the impact angle of the interplanetary shock had a significant impact on the occurrence rate and properties of Pc5 waves observed by high-latitude ground magnetometers.

Effect of Interplanetary Shock Impact Angle on the Occurrence Rate and Properties of Pc5 Waves Observed by High-Latitude Ground Magnetometers

Andrew Ballard Baker

GENERAL AUDIENCE ABSTRACT

Interplanetary shocks, drive interactions between the solar wind and the Earth's atmosphere, and they have the potential to have far reaching consequences. Caused by a variety of solar events including both Coronal Mass Ejections (CMEs) and Co-rotating Interaction Regions (CIRs), they have the ability to physically move the locations of regional boundaries of the ionized part of Earth's atmosphere, leading to a variety of electromagnetic effects. They also pose a danger at the human level by generating electrical currents in technological infrastructure that can overload transformers, communication cables, and power grids. As they pose a danger to our society, understanding them is prudent. A large portion of the current research into their behaviors has been focused on models and simulations and has shown that the shock impact angle should affect the properties of the waves. For this investigation, data from a series of Antarctic sensors was collected and compared to a database of known interplanetary shocks to determine when different shocks were detected. Specifically, for our investigation, we were concerned with determining what impact if any, the impact angle of the IP shock had on the generation of Pc5 waves, a specific type of ULF wave. This was accomplished by calculating the power level at different frequencies both before and after the shock. This information was then combined with the shock impact angle to determine what effects if any, the shock impact angle had on Pc5 wave occurrence rates. From our research we found that the impact angle of the interplanetary shock had a significant impact on the generation of Pc5 waves

Table of Contents

List of Tables

Table of Figures

Chapter 1

Introduction

Does the Interplanetary Shock Impact Angle Affect the Occurrence rate of Pc5 waves observed by high-latitude ground magnetometers? While interesting in their own right, Interplanetary (IP) Shocks by their nature are capable of having far reaching implications beyond simple scientific curiosity. They are examples of nonlinear waves in a collisionless plasma, and are a direct consequence of a variety of solar events including Coronal Mass Ejections (CMEs) and Co-rotating Interaction Regions (CIRs) [1]. In fact, the plasma dynamic pressure generated by these events can shift the bow shock and magnetopause Earthward. This can generate currents able to couple with the ionosphere, the ring current, and terrestrial power cables. In addition, shocks can "inject large numbers of energetic particles into Earth's inner magnetosphere, worsening the radiation environment for spacecraft and increasing the ring current" [2].

From a strictly conceptual standpoint, it makes sense that the effects of different IP shocks would depend on their impact angle. Consider the following two analogies. First, let us consider for a moment, the seasons of the Earth as felt in the northern hemisphere. How can we explain the seasonal temperature difference when we can show that the Earth-Sun distance isn't the main cause? One word, angles. Because the Earth's axis of rotation is tilted from perpendicular to the plane of the ecliptic by 23.5 degrees, the incidence angle of sunlight on the Earth's surface varies depending on the Earth's location in its orbit (This is also why it is summer in the southern hemisphere while it is winter in the northern hemisphere). As can be seen in figure 1 below, in winter, the northern hemisphere receives less sunlight than the southern hemisphere.

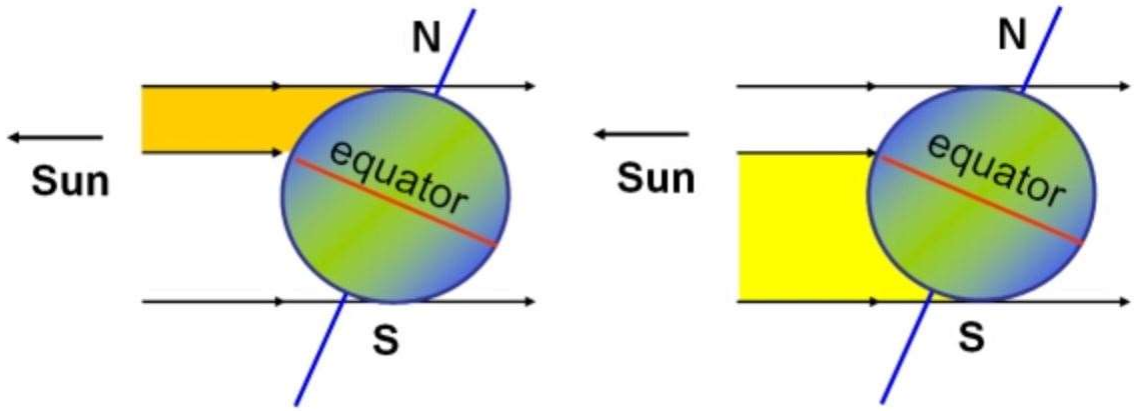

Figure 1: Winter in Northern Hemisphere (Left) and Summer in Southern Hemisphere (Right) [3]

What sunlight it does receive spreads out more and diffuses over a larger area due to the Earth's tilt (figure 2). In more technical terms, the flux of incident solar radiation decreases as a constant

quantity of sunlight must illuminate a larger area of the Earth's surface. The temperature fluctuations of the seasons clearly demonstrate the effect different incidence angles can have.

The same could be true for inclined shocks, as more energy would go to the hemisphere that is hit first. It's important to remember however, that inclined shocks transport less energy overall when compared to frontal shocks, as frontal shocks exert maximum pressure at the subpolar point, thereby maximizing energy transport.

This is similar conceptually to the idea brought forth in Oliveira and Raeder 2014 in which frontal shocks are more geoeffective because as the shock normal is aligned with the Earth-Sun line, they compress the subpolar magnetopause more strongly as they can exert a larger dynamic pressure when compared to an inclined shock. Moreover, frontal shocks compress the magnetosphere from all sides while inclined shocks push the plasma sheet either northward or southward, and as a result, it does not experience much compression [4].

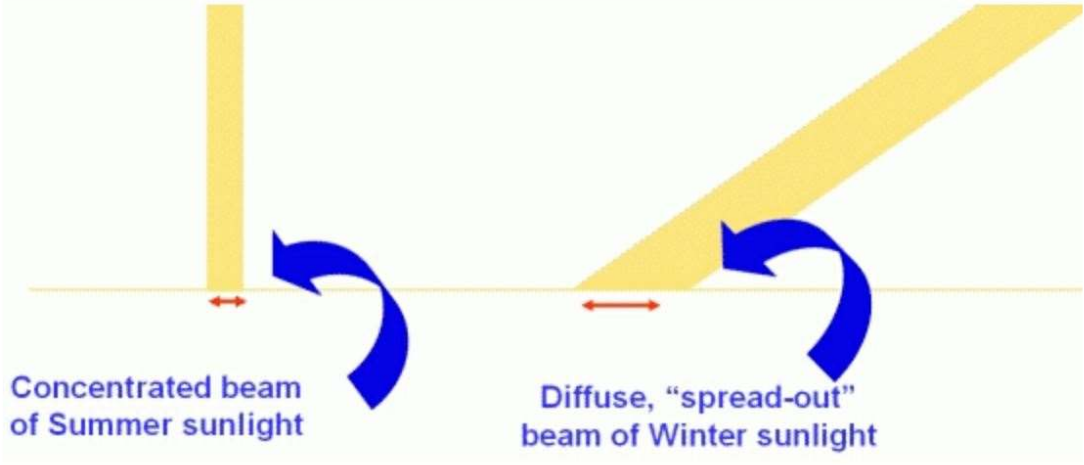

Figure 2: Diffusion of Sunlight with Perpendicular Impact (Left) and Inclined Impact (Right) [3]

For a second analogy let us consider a pebble dropped into a pond. When the pebble breaks the surface of the water, ripples are produced and expand radially outward away from the stone. Because of the conservation of energy, as the ripples expand outward, they decrease in magnitude before effectively ceasing to exist after traveling a large distance from their source (figure 3 below). This idea can be applied to Ultra Low Frequency (ULF) waves excited by IP shocks. If the shocks are inclined and have impact angles such that they are normal to a point in the northern hemisphere, their effects could be partially diminished by distance by the time they are detected by Antarctic magnetometers in the southern hemisphere. Similarly, if the shocks are inclined such that they have impact angles normal to a point in the southern hemisphere, they could be detected by Antarctic magnetometers more strongly as they would have had less distance to travel over which they could dissipate. Similarly, inclined shocks impact at different times at different locations, allowing some of the compressive results of their impact to dissipate before the entire impact has occurred.

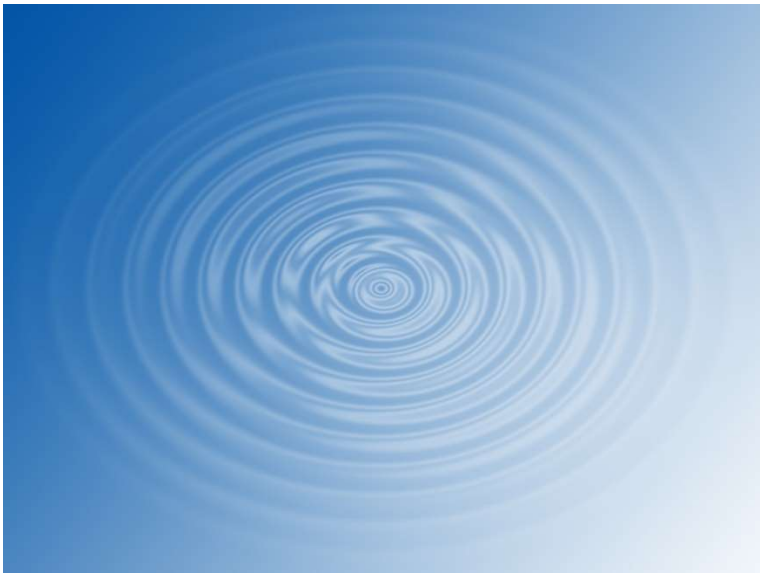

Figure 3: Ripples Expanding Radially with Decreasing Magnitude [5]

Before we begin, it is necessary to provide some background information in order understand some of the other events and processes that occur and to put this research into context.

1.1 The Sun

The sun is a giant ball of plasma in the center of the solar system. Its temperature varies widely depending on location. In the core of the sun the temperature is on the order of 15e6 K while the temperature on the visible surface is on the order of 5,000 K. Interestingly, the temperature again rises to around 10e6 K before again falling as you increase in height in the corona (the upper atmosphere of the sun) [6]. This is important because the solar wind is generated in the corona meaning that fluctuations and events here can have a significant impact on the properties of the solar wind as it propagates throughout the solar system.

1.2 Solar Wind

Resulting from the pressure differential between the solar corona and interplanetary/interstellar space, the solar wind can be viewed simply as the outward flow of the solar plasma.

The solar wind is composed of charged particles ejected from the corona. These charged particles, primarily consisting of electrons and ions in equal numbers (with smaller quantities of helium and other heavier elements relative to hydrogen atoms) have a wide range of velocities depending on their temperature but typically are around 400 km/s near the Earth [6].

The solar wind can generally be put into two different categories, the fast solar wind, and the slow solar wind. The slow solar wind is mainly generated through the thermal motion of particles in the sun's atmosphere. The fast solar wind on the other hand is generated when plasma is released upon magnetic reconnection in coronal holes.

The idea of a solar wind was first brought forward in the 1950's when it was noticed that variations in geomagnetic activity coincided with events observed on the sun.

In 1958 Parker became the first person to describe a model for the solar wind in his 1958 paper [7], where he demonstrated that if the suns equilibrium state was found, there must be a solar wind [6].

The radial-momentum flux (dynamic pressure) of the solar wind is of special interest because of its ability to confine the magnetospheric magnetic field [6].

It has been shown that the typical solar wind velocity at a distance of 1 A.U. is around 400 km/s. Similarly, the speed of sound at 1 A.U. is about 60 km/s. This clearly shows that the solar wind is supersonic [6]. This can lead to some interesting effects as a shock could be defined as the boundary between two locations with differing velocities and pressures (think of the shock that occurs when a plane transitions from subsonic to supersonic flight). We also know that the velocity of the solar wind decreases when it enters the influence of the Earth's environment. The end result of this, which will be discussed later, is that a shock will occur when the solar wind undergoes a transition from supersonic to subsonic velocities.

In addition, the inclusion of a magnetic field in the solar wind, can lead to hydromagnetic effects as the magnetic field exerts a pressure on the wind. Interestingly, this magnetic pressure is on the order of the gas pressure, implying that the effects of both of these pressures are important for the solar wind and any research in this area must take both of these pressures into account [6].

1.3 Interplanetary Shocks

Shocks are locations where the interplanetary plasma and magnetic field go through changes in density, temperature, field strength, and flow speed. When combined with the collisionless nature of space plasmas and the various wave modes, a variety of different shock types are generated. In a normal gas, shocks serve to transfer momentum and energy between molecules. In a collisionless plasma such as the solar wind, the mean free path of the particle is greater than the size of the system. This means that the aforementioned transfer of momentum and energy does not take place. To put this in perspective, the mean free path of the solar wind is on the order of 1 A.U. (1.5e8 km) while the thickness of the Earth's bow shock is 100-1000 km.

Simply put, shocks involve the speed at which information can be transferred, the response of an output to its input (nonlinear if not proportional), and dissipation. The velocity of the shock

creates an information horizon, behind which, the information is known and ahead of which, the 'update' has not yet reached.

If an object moves faster than the speed of sound in the medium, there must be a wave to propagate this information moving faster than the speed of sound. This is possible because an ordinary wave undergoes a reversable process (i.e. the compression is adiabatic without any dissipation). In the case of the supersonic wave, this is not the case. If the compression is not reversable, the entropy of the wave will increase which implies that the wave will dissipate [6]. This also implies that whatever the wave does to the gas will change its state (its density, temperature, or some other property will be changed). This supersonic wave is a shock wave.

In the reference frame where the shock is stationary, the direction that has not yet received information is the upstream or low-entropy side. Gas entering this side is supersonic. The other side of the shock is the downstream or high-entropy side. Gas leaving this side is subsonic. This means that in order for the conservation of mass to be true, the density of the gas must change which will alter its speed of sound.

Because the mass, energy, and momentum are conserved, MHD can be used to relate the upstream and downstream sides of the shocks. The relations between these two sides were first derived by Rankine and Hugoniot during the 19th century. For a collisional gas, the Rankine-Hugoniot relations (see below) uniquely determine the downstream state in terms of the upstream state.

The Rankine-Hugoniot Relations:

$$\frac{U_u}{\rho_u} - \frac{U_d}{\rho_d} + \frac{1}{2}\left(\frac{1}{\rho_u} - \frac{1}{\rho_d}\right)\left((\rho_u + \rho_d) + \frac{(B_{tu} - B_{td})^2}{2\mu_0}\right) = 0 \quad (1)$$

$$(\rho U_n)^2 \left[\frac{B_t}{\rho}\right] = \left(\frac{B_n^2}{\mu_0}\right)[B_t] \quad (2)$$

$$\left(\frac{1}{\rho_u} - \frac{1}{\rho_d}\right)(\rho U_n)^2 = [\rho] + \left(\frac{B_t^2}{2\mu_0}\right) \quad (3)$$

$$[U_t] = \left(\frac{B_n}{\mu_0 \rho U_n}\right)[B_t] \quad (4)$$

Where "ρ" is the mass density, "U" is the internal energy per unit mass, and "B" is the magnetic field. The subscripts "u" and "d" specify the "upstream" and "downstream" regions, while "t", and "n" represent the "transverse", and "normal" components respectively.

For collisionless plasma, these conservation relations do not provide unique solutions for the downstream state in terms of the upstream state. This is because in order to determine how much the ions and electrons are heated while passing through the shock, we must understand the shock structure and how it works.

1.4 Coronal Mass Ejections

One of the solar events than can generate an IP shock is a Coronal Mass Ejection (CME). CMEs are large releases of plasma and the associated magnetic field from the corona of the Sun. CMEs are capable of releasing billions of tons of material which carry a magnetic field that is frozen in flux. These magnetic fields are far stronger than the background magnetic fields typically found in the solar wind. They are capable of reaching the Earth in a timeframe ranging from less than a day to several days and expand as they propagate through space [8].

CMEs are created through a process of "magnetic reconnection" as shown in figure 4 below, where magnetic field lines become highly stressed and twisted before breaking and rearranging when two oppositely directed magnetic fields are brought together.

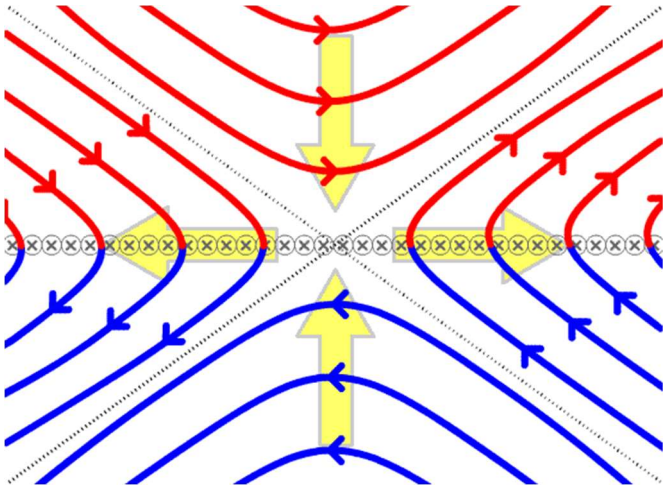

Figure 4: Magnetic Reconnection [9]

This snapping and reconnection of the magnetic field lines releases a tremendous amount of energy stored in the magnetic field and converts it into kinetic energy, thermal energy, and particle acceleration, which propel the plasma and magnetic field into space. If the CME travels faster than the background solar wind, a shock can be generated [8] [10].

This magnetic reconnection typically takes place in active regions such as sunspot groups or from locations where cooler dense plasma is trapped in the corona by magnetic flux [8]. CME production is also highly dependent on the solar cycle, being much more common near solar maximum [11].

As CMEs have a much stronger magnetic field relative to other solar wind structures, they can produce events on a scale not typically seen with normal solar wind activity. This includes the generation of large electric currents in the Earth's magnetosphere and ionosphere. This can lead to disruptions of communications and GPS systems and in extreme cases, a failure of the power grid [12].

1.5 Co-rotating Interaction Regions

Another solar event that can generate an IP shock is a Co-rotating Interaction Region (CIR). A CIR is very much as its name suggests, a region where a fast solar wind stream caused by a coronal hole interacts with a slow solar wind stream to produce a CIR in interplanetary space [13] [14] [15]. They are capable of producing geomagnetic storms when they reach the Earth [14].

Generally speaking, the lower velocities of the slow solar wind allow for its magnetic field lines to be more curved than those of the fast solar wind [13]. This curvature of the magnetic field lines causes these regions to have spiral shapes that can wrap around the sun as they corotate with the sun [16]. This spiral shape, along with several other characteristics of CIRs is clearly visible in figure 5 below.

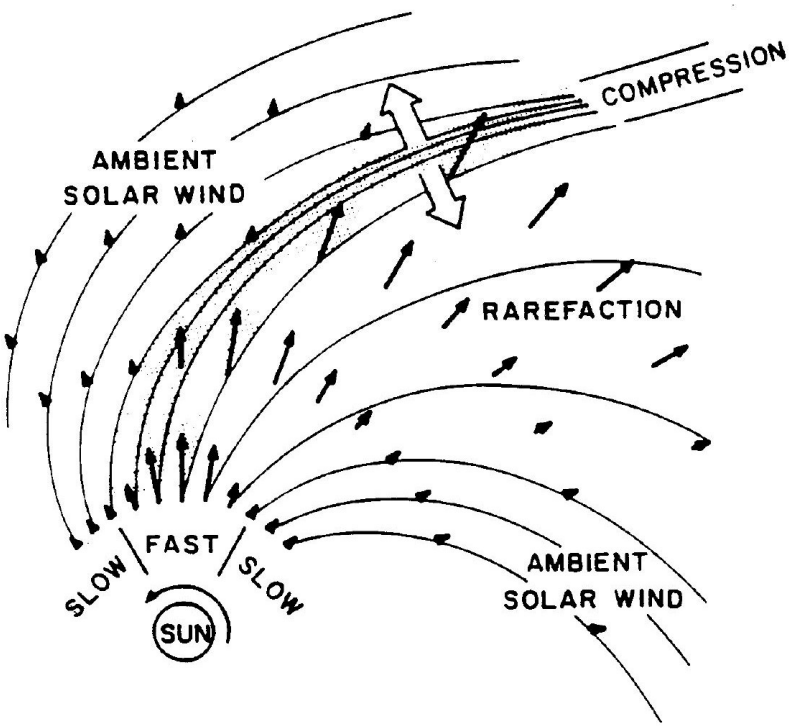

Figure 5: Co-rotating Interaction Region with Fast and Slow Regions causing Characteristic Spiral Shape in the Ambient Solar Wind with Rarefied and Compressed Regions [17]

CIRs have several notable characteristics which are clearly visible in figure 5. The first is that as the fast stream catches up with the slow stream ambient solar wind, it forms a compression region in the rear of the slow stream. As the fast solar wind is emitted from a rotating source, this compression region takes the characteristic spiral shape mentioned previously. The second is the high probability of this compression region producing a shock (both a forward shock and a reverse shock). The third notable characteristic is the generation of a rarefied region in the back of the fast stream [16]. This rarefied region is created as the fast solar wind essentially pushes

the slow solar wind out of the way while the slow solar wind which is by definition slower, cannot reenter the region at a high enough rate to maintain the pressure.

1.6 Magnetosphere

A magnetosphere is a region of space around an astronomical object where the dominant magnetic field is that of the object instead of that of the solar wind. As discussed earlier, the solar wind imparts a pressure on the Earth's magnetic field. This causes the magnetosphere to take a distinctive shape, in which the side facing the sun is compressed, and the side facing away from the sun is stretched into an elongated tail [18]. In addition, as the pressure exerted by the solar wind can vary with time, the magnetosphere expands and contracts with decreasing and increasing solar wind pressure respectively. As discussed previously, as the solar wind is supersonic, it travels far faster than any pressure wave that could divert it. As this wave does not have the velocity to move upstream, it forms a nonlinear fast magnetosonic shock front between the solar wind and the magnetopause [6].

This shock front, called the Bow Shock is the outer layer of the magnetosphere. It is the boundary layer between the magnetosphere and interplanetary space. It is also the location where the velocity of the solar wind decreases to subsonic velocities, and many of the charged particles of the solar wind are deflected around the Earth [6], [19].

The magnetosheath is the region between the bow shock and the magnetopause. It is formed primarily from the solar wind after it has passed through the bow shock. The direction and magnitude of the magnetic field are highly variable in this region.

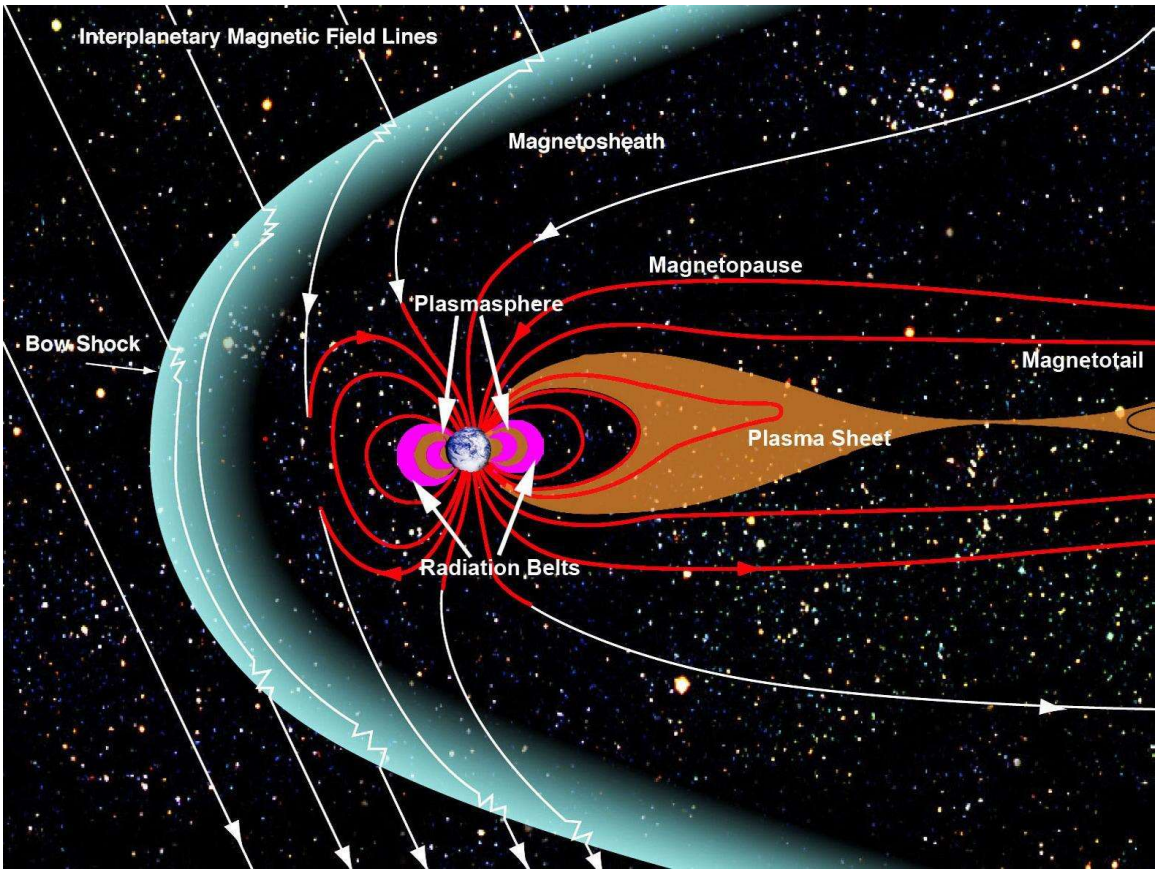

Figure 6: Diagram of the Magnetosphere Depicting Bow Shock Interactions with the Magnetosphere. [19]

The magnetopause is the equilibrium position of the magnetosphere where the pressures of the planetary magnetic field and the solar wind are the same. The size and shape of this layer are variable with the pressure from the solar wind.

The magnetotail is the component of the magnetosphere on the other side of the planet from the shock (the night side). Containing both a northern and southern lobe, the magnetic field lines in the northern lobe point towards the object while those in the southern lobe point away. These two lobes are separated by a plasma sheet.

Figure 6 above provides an example of how the various parts of the magnetosphere interact with the interplanetary magnetic field lines and clearly shows how they become bent and distorted as they interact with the tear drop shaped magnetosphere.

1.7 Ionosphere

The Ionosphere is the ionized part of the Earth's upper atmosphere at an altitude of 60 km – 1000 km. There are several methods in which particles in this region become ionized. These include photons (photoionization) and energetic particles (impact ionization). While the photons mostly come from the sun, the ionized particles come from a variety of sources including cosmic rays

from the galaxy, the sun, the magnetosphere, or the ionosphere itself. Bremsstrahlung (breaking radiation) caused by precipitating electrons can produce additional ionizing photons within the ionosphere itself. While multiple sources produce the ionization found in the ionosphere, usually one source dominates. Typically, solar EUV and UV (10 nm to 100 nm) are primarily responsible for the production of the dayside ionospheres of most planets [6].

1.8 Plasma Waves

1.8.1 Compression Waves

Generally, waves are divided into two broad categories based on their types. The first group is composed of mechanical type waves as would reasonably be expected to occur in a gas due to particle interactions and are responsible for the transmission of sound. Compression waves are examples of this type and are depicted by figure 7 below. Figure 7 depicts compressed pulses traveling along a spring separated by rarefactions caused by the temporary movement of particles as the wave propagates through the spring.

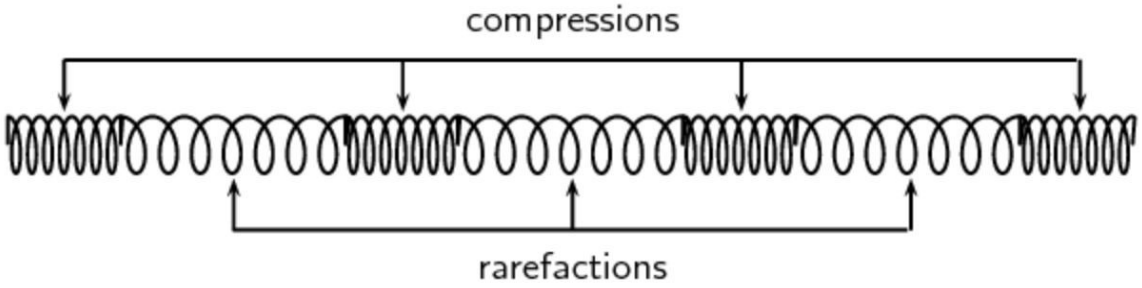

Figure 7: Compression Waves – A Type of Mechanical Waves depicted on a spring [20]

1.8.2 Electromagnetic Waves

The second category belongs to electromagnetic waves which propagate through space with a varying electromagnetic field. An example of which is depicted by figure 8 below.

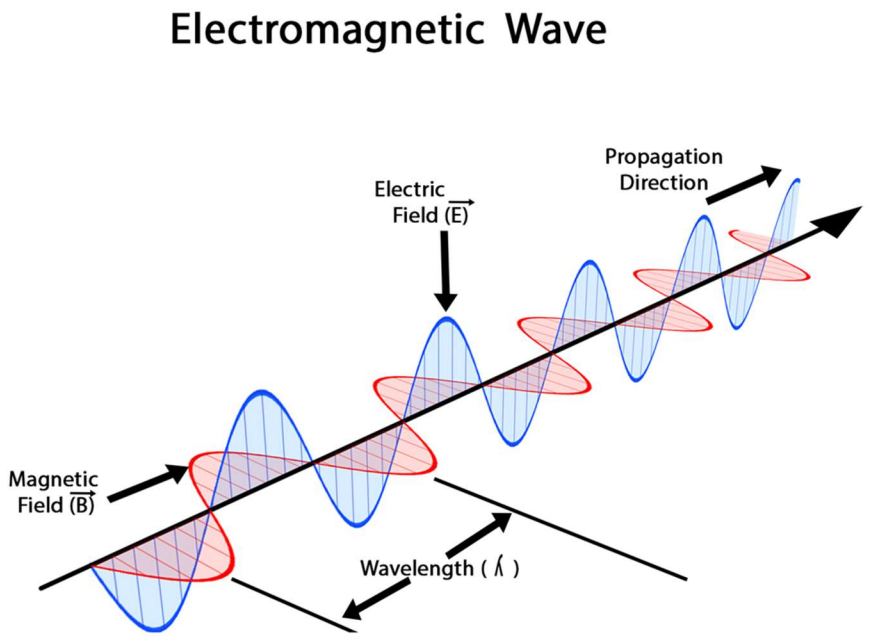

Figure 8: Electromagnetic Wave with Perpendicular Electric and Magnetic Components [21]

As figure 8 demonstrates, an electromagnetic wave consists of both an electric component and a magnetic component which vary in amplitude over time and are perpendicular both to each other, as well as the propagation direction of the wave.

Plasma waves however are distinct from both of these types. On one hand plasmas are composed of particles and can behave like the mechanical waves of the first group as density and pressure must be considered as the particles directly interact with each other. On the other hand, these particles are charged particles and can carry currents, allowing for the propagation of electromagnetic waves, meaning the particles can interact with each other over large distances. Thus, plasma (or more specifically magnetohydrodynamic (MHD)) waves have properties of both mechanical and electromagnetic waves and behave differently from the traditional two types mentioned above and instead behave as a hybrid, displaying properties of both types. It should be noted however that while every MHD wave is a plasma wave, not all plasma waves are MHD waves [6].

1.8.3 Alfvén Waves and ULF Waves

Named in honor of Hannes Alfvén, the first person to describe them, Alfvén waves are a subset of MHD waves where ion oscillation is induced by a restoring force generated by the effective tension of the magnetic field lines (i.e. the force which attempts to straighten bent magnetic field lines). Alfvén waves are one wave solution to the dispersion relations for an MHD plasma. Two of the classes of these solutions are compressional and carry "changes of plasma and magnetic pressure and changes of plasma density" [6]. The third type of Alfvén wave on the other hand does not change the plasma pressure or density but rather only bends the magnetic field lines.

This type is called a *shear Alfvén wave*. Another related type of Alfvén wave is called the *standing Alfvén wave*. Standing Alfvén waves are classes of solutions to the MHD dispersion relation in a bounded media. They occur when there is a reflecting boundary condition at the ionosphere, which allows wave energy in the magnetosphere to bounce back and forth along the field lines between the ionosphere. This creates a standing wave solution with no net energy transfer. In contrast to compressional Alfvén waves, transverse waves can exchange energy with different frequencies in the plasma because their magnetic field changes perpendicularly with the direction of wave motion [22].

An illustration showing the importance of these waves and how they can impact the ground is given by figure 9 below. Figure 9 depicts ionospheric currents produced as a result of resonance effects. The original wave is a polarized Alfvén wave with field aligned currents. Pederson currents close the field aligned currents and effectively cancel out the impacts of the field aligned currents. On the ground, **J** x **B** effects produce a rotated magnetic field.

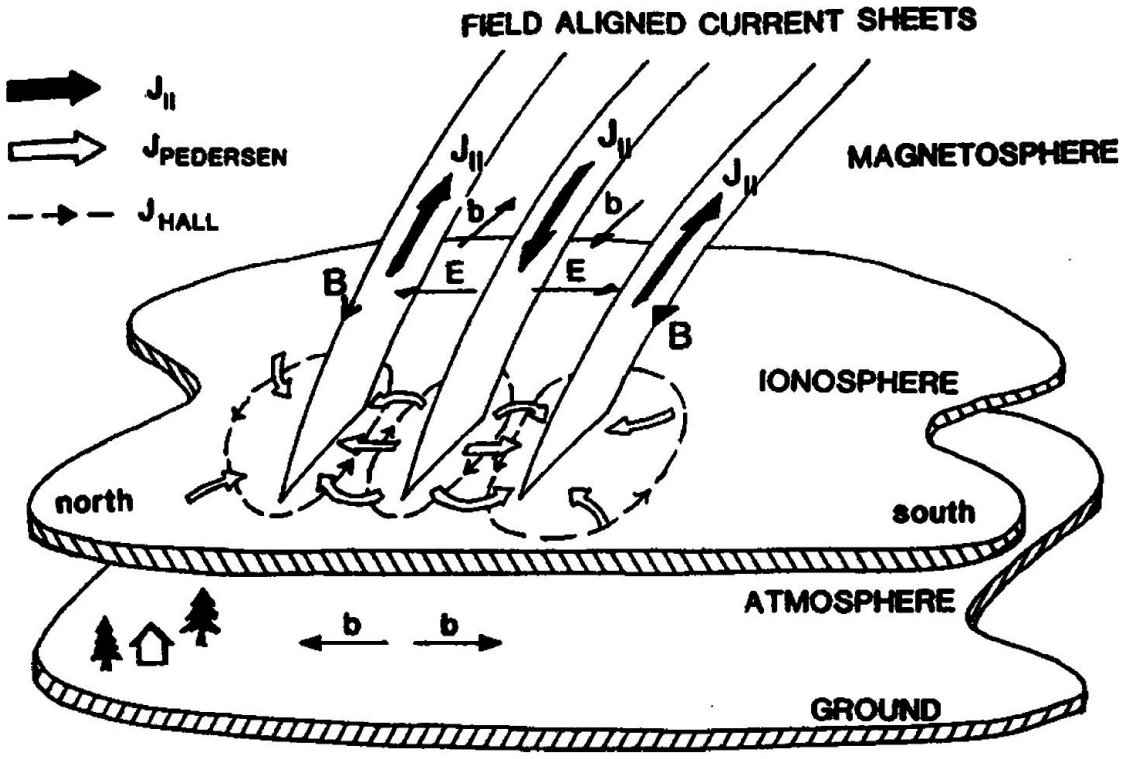

*Figure 9: Ionospheric currents produced as a result of resonance effects. The original wave is a polarized Alfvén wave with field aligned currents. Pederson currents close the field aligned currents and effectively cancel out the impacts of the field aligned currents. On the ground, **J** x **B** effects produce a rotated magnetic field [23]*

In magnetospheric science, Ultra-Low Frequency (ULF) waves are waves with a frequency range around 1 mHz to 5 Hz [24]. Additionally, for the definition of a "low frequency", the frequency in question must be lower than the natural frequencies of the plasma such as the plasma frequency and the ion gyrofrequency.

During early studies of these waves, it was determined that these ULF waves can be divided into several different categories based on substantial differences between them. One of these groups called "continuous pulsations" (Pc) have a quasi-sinusoidal form and a well-defined spectral peak. These can be further divided into subgroups based on their frequencies and periods. These range from Pc-1 (0.2 – 5 Hz) to Pc-5 (1.7 – 6.7 mHz) [6], [25]. Another broad group was called "irregular pulsations" (Pi), and were characterized by having power at many different frequencies [6], [24].

Harmonic	Pattern	# of Loops	Length-Wavelength Relationship
1st	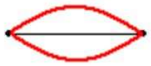	1	$L = 1/2 \bullet \lambda$
2nd	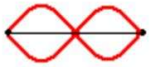	2	$L = 2/2 \bullet \lambda$
3rd	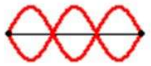	3	$L = 3/2 \bullet \lambda$
4th	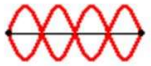	4	$L = 4/2 \bullet \lambda$
5th	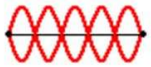	5	$L = 5/2 \bullet \lambda$
6th	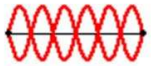	6	$L = 6/2 \bullet \lambda$
nth	--	n	$L = n/2 \bullet \lambda$

Figure 10: Standing Waves Harmonics on a String. From left, the first column shows the harmonic, the second column shows the associated pattern. The third column shows the number of loops in each harmonic and the fourth column describes the relationship between the length and the wavelength. [26]

Oscillating magnetic fields on the Earth's surface can be explained by MHD waves in the ionosphere and magnetosphere. What's more, distinct periods of Pc pulsations suggest a resonant process. This process is similar to the "standing wave on a string" (figure 10 above) example used in introductory physics classes and can contain even and odd modes (figure 11 below) as well as various harmonics demonstrated in figure 10. These pulsations are caused by standing Alfvén waves along the Earth's magnetic field lines, which, as previously mentioned, bounce back and forth in the ionosphere between reflecting boundary conditions, resulting in a standing wave solution with no net energy transfer.

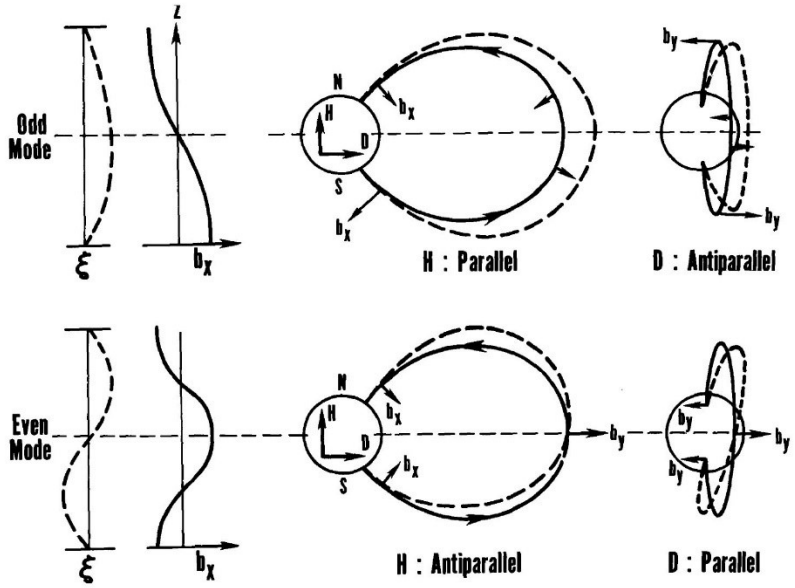

Figure 11: Even/Odd Wave Modes of a regular dipole. The top panel represents odd modes while the bottom panel represents even modes. The left panel is analogous to a representation of the middle panel using stretched strings. The middle panel depicts the magnetic field lines of a regular dipole. The dipole field lines are capable of oscillating in two directions (radially in the case of the center panel, and azimuthally in the case of the right panel). The center and right panels also show how the ends of the field lines are anchored by the ionosphere, and act as nodes of field line displacement and antinodes of the magnetic perturbation. [23]

The middle panel of figure 11 above depicts the magnetic field lines of a regular dipole. In order to visualize the differences that arise due to whether we are looking at an even mode (bottom) or an odd mode (top), the left panel is analogous to a representation of the middle panel using stretched strings. This is similar in concept to the patterns and harmonics depicted in figure 10. Additionally, the dipole field lines are capable of oscillating in two directions (radially in the case of the center panel, and azimuthally in the case of the right panel). The center and right panels also show how the ends of the field lines are anchored by the ionosphere, and act as nodes of field line displacement and antinodes of the magnetic perturbation [23].

A significant difference from the symmetric dipole and symmetric standing wave solutions envisioned in Figure 11, however, is illustrated in Figure 12 below, where a regular magnetic dipole is depicted in comparison to the magnetosphere under pressure from the solar wind. This pressure clearly compresses and distorts the magnetic field into the familiar tear drop shape taught in basic astronomy classes. Because of this distortion, it seems plausible that asymmetric solar wind driving conditions could affect standing wave solutions and ULF wave activity.

Additionally, as larger field line displacements occur at the equator with odd harmonics, which benefit frontal shocks, and larger field line displacements occur off the equator with even harmonics, which benefit inclined shocks, it seems plausible that inclined shocks and frontal shocks are likely to excite different harmonics.

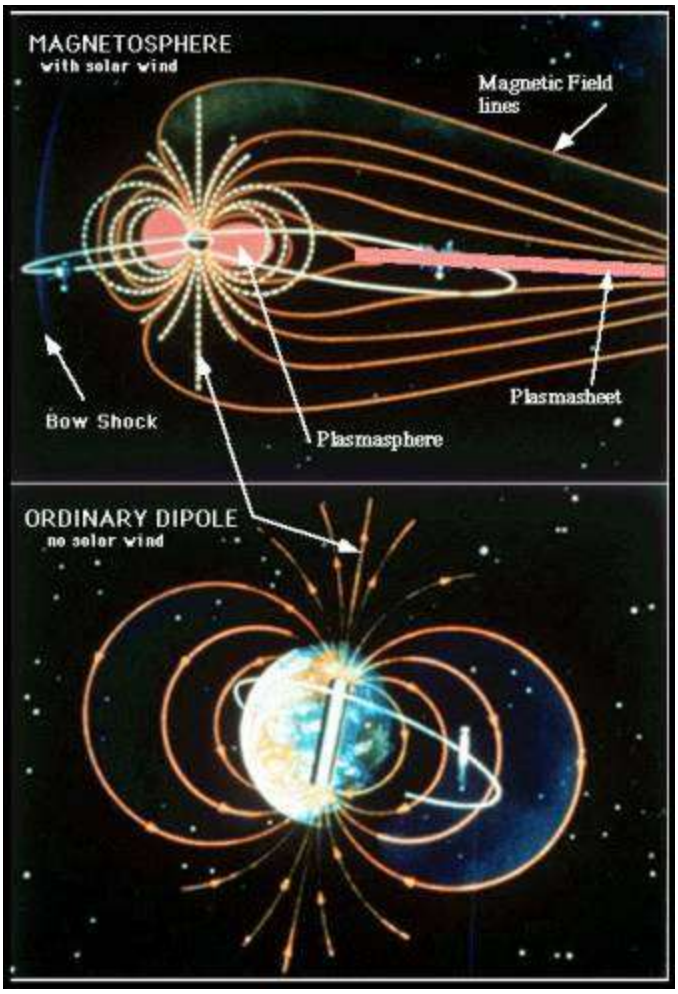

Figure 12: Earth's Magnetic Field with (top panel) and without (bottom panel) the Solar Wind [27]

1.9 Existing Research: The Relationship Between IP Shock Angle and ULF Wave Generation

While there has been prior research looking into the geoeffectiveness of shocks at varying impact angles, it has mostly been performed either through the use of simulations with a lack of real measurements or with data collected from satellite missions as opposed to data directly measured on the ground.

Oliveira and Raeder 2014 showed that the angle of the shock with respect to the Earth-Sun line impacts the global magnetosphere-ionosphere systems response, including ULF wave activity. These simulations indicate that ULF wave properties should be affected by IP shock angle, however this has not been tested with measurements [4].

The result of this simulation can be seen in figure 13 below, which shows magnetic perturbations and is oriented to depict the xz GSE plane. It demonstrates the expected propagation of both an inclined shock (left) and a frontal shock (right) through time. It also provides a good visualization of why it is expected that frontal shocks are more geoeffective than inclined shocks as frontal shocks send waves symmetrically into the magnetosphere which compress the plasma sheet when they converge from all sides. Inclined shocks on the other hand, produce waves that impact the plasma sheet at different times, reducing the compression and instead shifting it northward or southward [4].

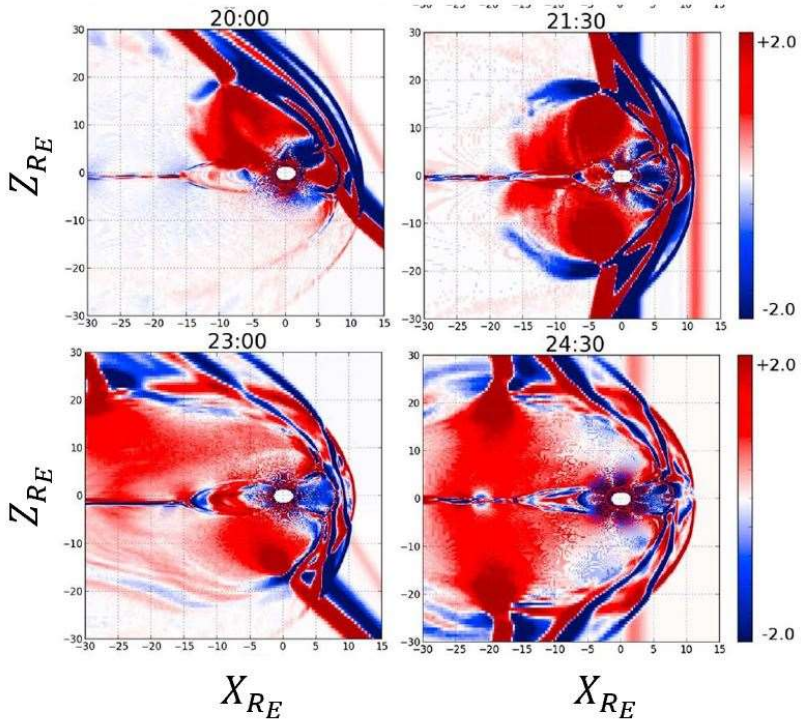

Figure 13: Oliveira and Raeder 2014 Shock Impact Angle Simulation showing ΔB(nT) plotted in the meridian plane with the x-axis representing X_{R_E} and the y-axis representing Z_{R_E} The left panel depicts the impact of an inclined shock while the right panel depicts the impact of a frontal shock. The time of the simulation increases in the lower panels. [4]

In Oliveira and Raeder 2015, data from the Wind and ACE satellites was used to analyze the geoeffectiveness of IP shocks due to their impact angles. These results matched those of their earlier simulations in 2014, finding that the impact angle of the IP shock is just as important as the shock strength itself in determining it's geoeffectiveness. They believe this relation is due to the same wave compression symmetry they described in 2014, allowing for energy stored in the magnetotail to be released, producing auroral substorms observed on the ground [28].

Studies such as these directly inspired the research to be discussed below. As they focus on simulations or measurements taken by satellites, they lack direct ground measured data for verification. The MIST Antarctic magnetometers provided a unique opportunity to experimentally validate these theories. The placement of the magnetometers at extreme northern or southern latitudes enables the best possible measurements of the differences between frontal

and inclined shocks as due to the curvature of the Earth, the time delay of the impact of an inclined shock on a globally conjugate region would be maximized. This led to the formation of the question to be investigated below, namely "Does interplanetary shock impact angle affect the occurrence rate of Pc5 waves observed by high-latitude ground magnetometers?". This investigation also differs from previous research in that it looks at ULF waves (specifically those in the Pc5 range) while studies such as those conducted by Oliveira and Raeder focus on the overall global implications of the shocks.

Chapter 2

Methodology

2.1 Antarctic Research

Magnetometer data was obtained from several Antarctic ground stations operated by the Magnetosphere – Ionosphere Science Team (MIST) at Virginia Tech [29]. MIST is a part of the Space Physics Research Group at Virginia Tech and investigates the interaction between the Earth's magnetosphere and its ionosphere.

MIST operates several magnetometers on the Antarctic Plateau as shown in figures 14 and 15 below that collect data at a sample frequency of 1 Hz. The locations of these magnetometers were chosen as they are magnetically conjugate to others on the western Greenland coast and complete the PENGUIn (Polar Experimental Network for Geospace Upper atmosphere Investigation) 40-degree magnetic meridian chain.

AAL-PIP Station	Geog. Lat.	Geo. Long (E)
PG0	-83.670065	88.680650
PG1*	-84.50	77.20
PG2	-84.418598	57.955558
PG3	-84.810127	37.629373
PG4	-83.339908	12.252648
PG5	-81.961297	5.71129

*No housekeeping data.

Figure 14: MIST Magnetometer Locations

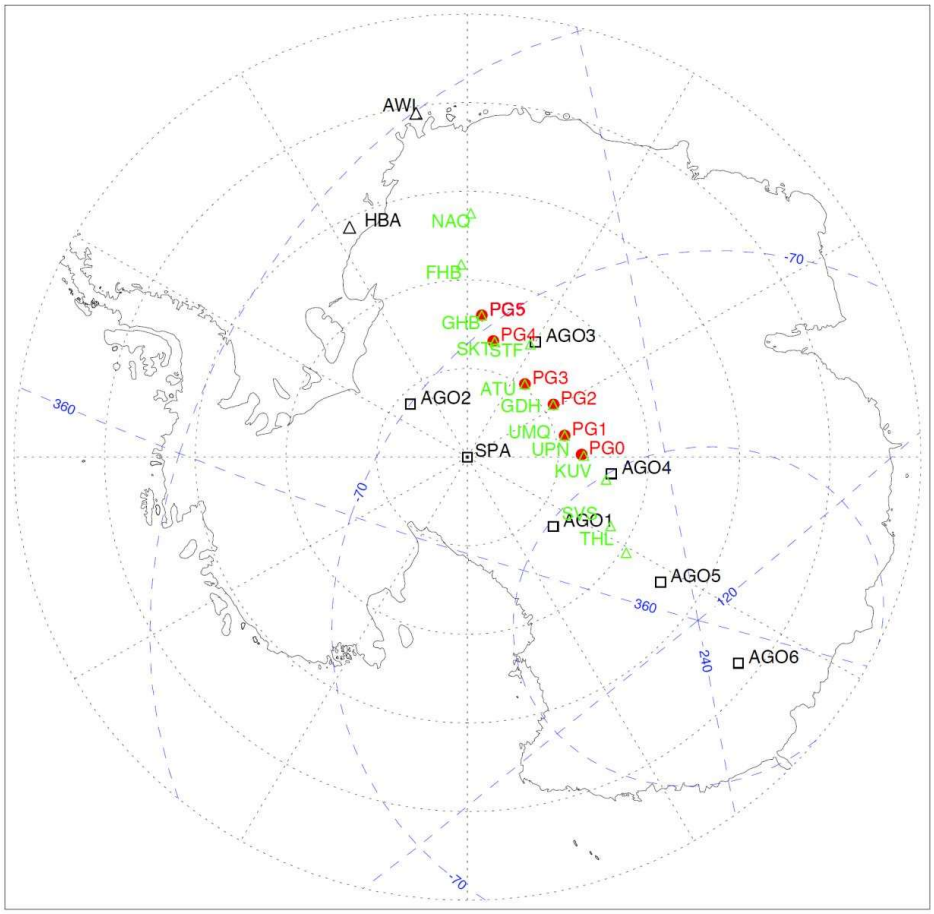

Figure 15: Map of MIST Magnetometer Locations (red) and other magnetometers

The 2018 Oliveira Shock Database was used as a reference for the detection times, impact angles, and velocities of the shocks [30]. Oliveira's shock database is comprised of 547 IP shocks detected between January 1995 and September 2017. The shock parameters given in the database were calculated through a combination of Wind and Advanced Composition Explorer (ACE) solar wind and interplanetary magnetic field (IMF) data as well as finding solutions of the Rankine-Hugoniot equations [30]. This was initially combined with MIST magnetometer data taken from the PG3 station for days in which a shock was detected (Other stations were added later).

2.2 Time Series

Time series plots were then created from this magnetometer data. Specifically, the magnetometer PG3 was used as it had been in operation for a while and had most likely detected multiple shocks. The resulting plots initially showed various trends in the data. As a result, the data was detrended by fitting a 3rd order polynomial to the data and subtracting it. This served to simplify further analysis and reveal information that would otherwise be hidden in the trend. A 3rd order polynomial was used as it effectively eliminated the observed trends and a higher order polynomial was determined to be overkill.

Figure 16 below shows the time series of the full 24 hours of January 18th, 2016. The top panel shows H[nT] which is aligned in the direction of magnetic north, the middle panel plots E[nT] which points towards magnetic east, the third panel plots Z[nT] which points towards the center of the Earth, and the bottom panel plots the magnitude as calculated by the following equation.

$$Magnitude = \sqrt{H[nT]^2 + E[nT]^2} \quad (5)$$

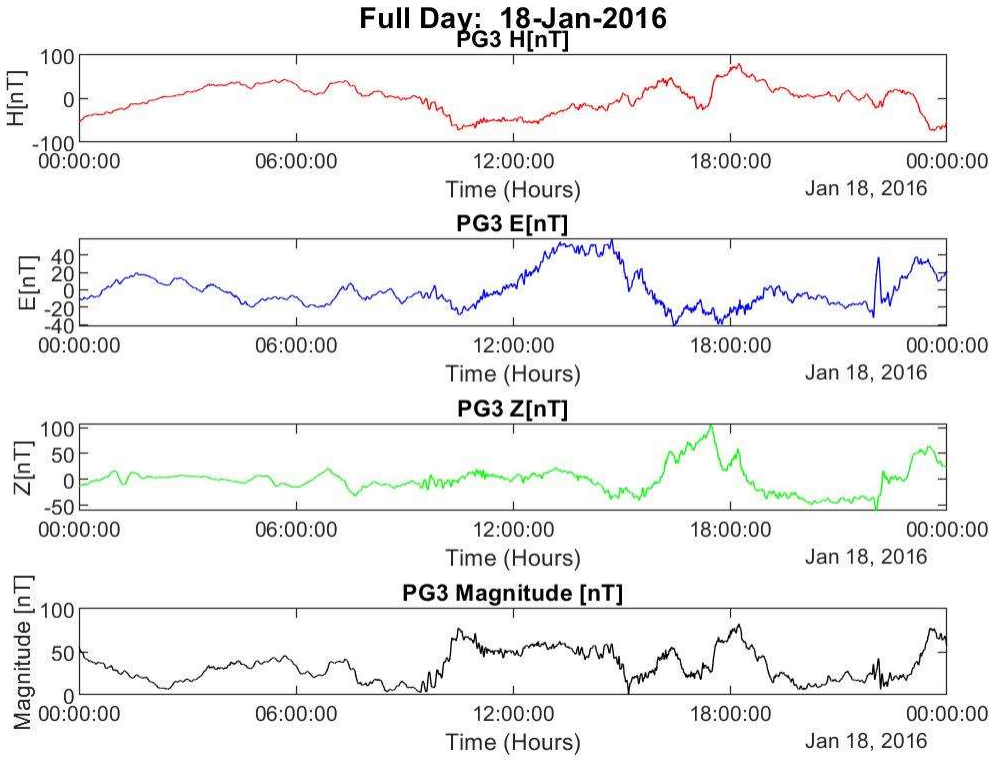

Figure 16: Full Day Time Series for January 18th, 2016. H[nT] (top), E[nT] (second from top), Z[nT] (third from top), Magnitude [nT] (bottom).

The 24 hour time series were then scaled to isolate only the time of the shocks taken from the Oliveira database with a 1 hour margin before and after the shock. This is shown in figure 17

below. The centered vertical blue line indicates the time of the shock given in the 2018 Oliveira database. In the case of January 18th, 2016, the shock time was given as 21:57 UTC. Local time was calculated by subtracting 2.5 hours from the UTC time giving the local time of 19:27 for the shock on January 18th, 2016.

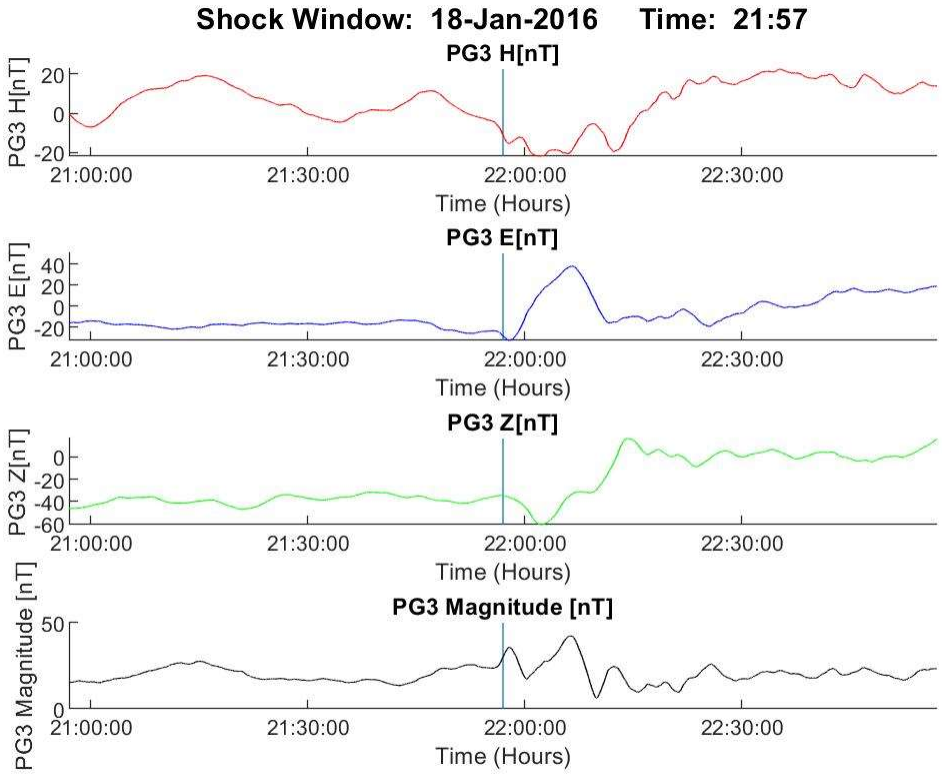

Figure 17: Hour Window Before and After Shock given by vertical blue line. H[nT] (top), E[nT] (second from top), Z[nT] (third from top), Magnitude [nT] (bottom).

The plots were then manually inspected to determine the shock time. This was done by examining the entire plot with particular emphasis placed on the time given in the Oliveira database and the magnitude plots. While the shocks do not always produce an obvious shape in the graphs, in general, the shock was determined by finding a sharp dip or bump in the H[nT], E[nT], and magnitude plots occurring around the time given in the Oliveira database. While this method is not foolproof, it was generally found that the detected shocks matched the time given in the Oliveira database.

2.3 OMNIWeb

As would be expected for this type of analysis, some shocks were easier to see than others. For shocks that were difficult to visually find in the magnetometer data, OMNIWeb data (shown in figure 18 below) was used as a supplement to determine the detected shock time.

OMNIWeb is a NASA database of various Low and High resolution solar wind data measured by a variety of spacecraft as well as other data frequently used with solar wind data such as proton fluxes and energies.

The Proton Density and SYM/H OMNIWeb data were plotted for the days in question and examined around the time of the shock from the Oliveira database. The proton density, as its name suggests, measures the density of protons (i.e. the number of protons per cubic centimeter). SYM/H on the other hand, is a measurement of the horizontal component of the magnetic field with a 1 minute time resolution. As can be seen in figure 18 below, for January 18th, 2016, there is a large jump in SYM/H around the time of the shock given in the Oliveira database. This was taken to be a confirmation of the shock time.

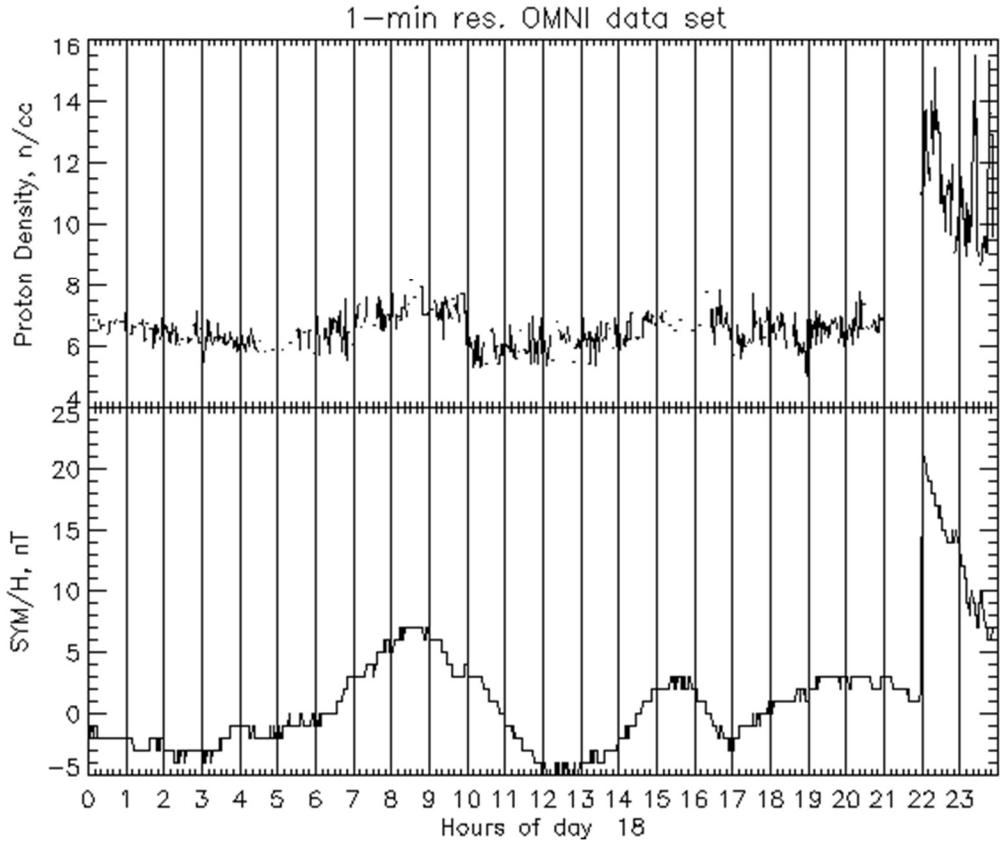

Figure 18: OMNIWeb Plot Depicting both Proton Density (top) and SYM/H (bottom)

2.4 Visual Examination

The time series plots of both the full day and the hour window around the shocks were also visually examined to determine if periodic waves had been generated as a result of the shock. This proved difficult as sometimes it was unclear whether or not waves had been generated or if the time series just gave the impression that they had been. In addition, some of the data in the time series could have hidden low amplitude periodic waves. For example, if one looks at the hour-long window time series above for January 18th, 2016, it is easy to see how waves occurring at 21:15 and 22:30 could be hidden in the H[nT] plot for PG3 if they are low in amplitude compared to the surrounding data. This is a significant reason why the data was detrended, as well as why the magnitude was calculated, and multiple sensors were observed as these increased the chances of being able to visually see any generated waves.

2.5 Power Spectra

In order to determine the power spectra, a Fourier analysis was then performed on the data. A Fourier analysis is a method of modeling a periodic waveform in terms of trigonometric functions. As many waveforms consist of energy at both a fundamental frequency and at various harmonic frequencies (multiples of the fundamental), the distribution of energy in the fundamental and harmonic frequencies determines the shape of the wave.

For this analysis, the pwelch function in MATLAB was used. Welch's method is a tool for estimating the power spectra of a signal. It is implemented by dividing the signal into multiple segments, estimating the spectral density of each segment, and averaging the results. Welch's method is an improvement over the standard signal spectral density estimates, in that it reduces noise in the estimated power spectra. Of course, with any gain there is downside. In this case, the improvement in noise reduction comes at the expense of a reduced frequency resolution.

It should also be noted that for the power spectra analysis, no discrimination is made between monochromatic wave activity and waves with a broadband frequency spectrum.

The power spectra before and after the shock were compared to find the percent difference. In order to eliminate any power fluctuations due to the shock itself and to focus on only the power before and after the shock, a five-minute window both before and after the shock was ignored for this analysis. To simplify the calculations, a 68-minute window was actually used above as the window size before and after the shock. As the five-minute period around the shock was ignored, the length of each Fourier transform window was 63 minutes.

Figure 19 below shows the Power Spectral Density (W/Hz) both before and after the shock as well as the percent difference between them for PG3. All the plots are logarithmically scaled. This means that a percent difference of 2 is actually a 100% difference when converted back to an integer and a percent difference of 3 is actually a 1000% difference.

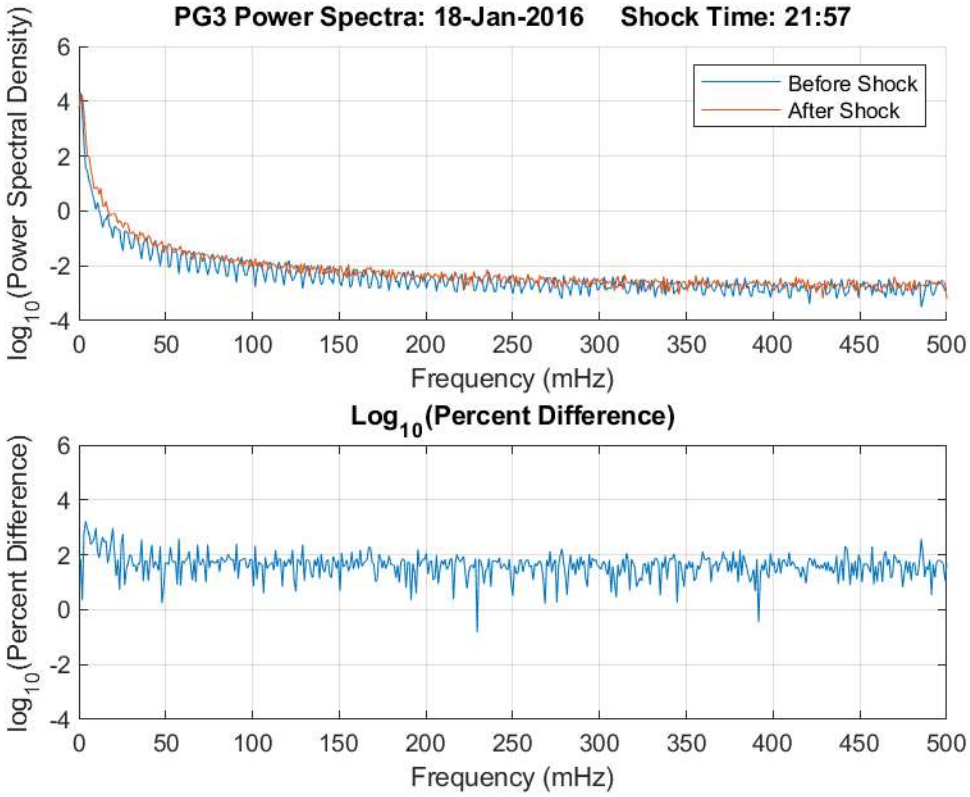

Figure 19: PG3 Power Spectra for January 18th, 2016. The top panel displays the log10 scaled power spectra at various frequencies. The power spectra before the shock is given by the blue line while the power spectra after the shock is given by the orange line. The bottom panel displays the log10 scaled percent difference between the two spectra in the top panel.

The figure above for PG3 shows the power spectra for both before the shock and after the shock (the blue and orange lines respectively in the top figure) as well as the log_{10} scaled percent difference (bottom figure) between the two up to a frequency of 500 mHz. While not always the case as will be shown with other examples later, the power spectral analysis indicates not only that there was generally more power after the shock at a given frequency, but that this power difference was significant.

This percent difference is illustrated in the second graph. While 500 mHz is significantly outside of the Pc5 range under investigation, its inclusion was considered important as it provides a greater context for the percent difference plots as well as allows for the observation and detection of interesting patterns and events that merit further research. This will be covered in more detail later. It is interesting to note that while the percent difference had significant fluctuations over the 0 mHz to 500 mHz frequency range, the general percent difference level stayed relatively unchanged. The percent difference was calculated using the following equation.

$$Percent\ Difference = log_{10}\left(\frac{Spectrum\ After - Spectru\quad Before}{Spectrum\ Before} * 100\right) \qquad (6)$$

The percent difference between the power spectra before and after the shock was used instead of the regular difference because it provided a more useful statistic that could be readily compared to other shocks, while the regular difference was highly dependent on the ambient power spectra at the time in question as well as the specific strength of a particular shock.

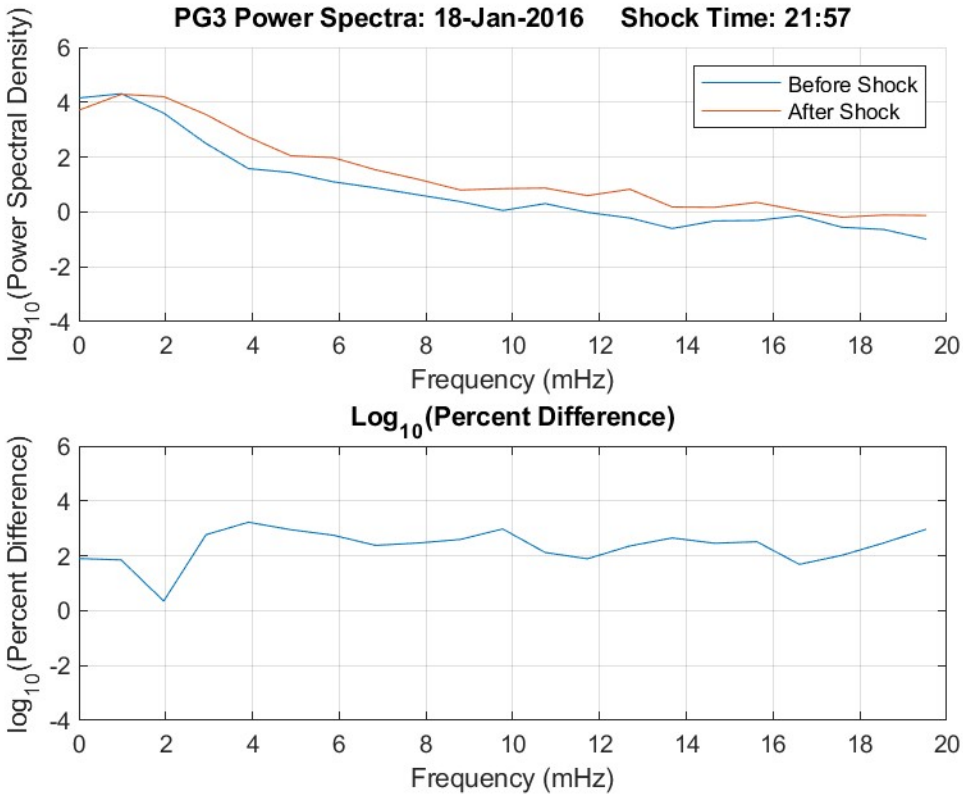

Figure 20: Pc5 Range Power Spectra for January 18th, 2016 PG3. The top panel displays the power spectra before the shock (blue) and after the shock (orange). The bottom panel shows the log10 scaled percent difference between the two spectra in the top panel.

Figure 20 above plots the same power spectral density and percent difference information for PG3 as the preceding plots in figure 19, however the x-axis has been scaled to allow for easy observation and analysis of the Pc5 range. It should be noted that the power spectra after the shock generally follows the patterns of the power spectra before the shock, only shifted in amplitude. It is also interesting to note, that with the exception of a jump in the percentage difference between the two spectra around 2 mHz, the percentage difference between the two does not vary significantly over the frequency range (on a logarithmic scale).

The above plots also indicate other differences between the two measurements. For example, at very low frequencies (i.e. less than 1 mHz), the power spectra measured by PG3 before the shock is actually larger than the spectra after the shock. This is most likely due to aliasing effects resulting from the length of the Fourier window. 1 mHz has a period of roughly 17 minutes, making it on the larger side. While the Fourier transform window has a length of 63 minutes,

this is only 3.7 times larger than the 17-minute period, meaning that aliasing effects could be experienced, and frequencies around this range are likely less reliable.

The remainder of the spectra follows the norm of the power spectra after the shock being larger than the spectra before the shock, meaning this discrepancy is surprising. This is especially true when the percent difference plot is examined. If one ignores the 0 – 1 mHz range as unreliable, the difference between the two spectra generally falls within a limited range. This implies that the frequency of the measurement does not significantly affect the measured percent difference of the power spectra before and after the shock.

2.6 Shock Table and Wave Observations

In order to keep track of each of the shocks detected by PG3 and conduct further wave analysis via visual inspection, an excel file was created. This file contained the standard information about which station detected the shock as well as the associated date and time, the shock angle, and its velocity. In addition, it also contained more individualized information including whether a visual analysis based on the time series above showed the existence of waves as well as the type of shock (such as whether the shock was generated by a CME, a CIR, or something else).

Table 1: Subset of Interplanetary Shock Information (see appendix for full table)

Ground Station	Date	Shock Time	Observed Shock Time	Local Time (UTC – 2.5)	Angle (degrees)	Velocity (km/s)	Waves	Oliveira Data	Shock Type
pg3	15-Feb-14	13:16	13:16	10:46	146.51	475.53	U	2018	CME
pg3	18-Feb-14	6:39	6:40	4:10	141.21	374.15	N	2018	CME
pg3	19-Feb-14	3:47	3:47	1:17	160.08	582.7	N	2018	CME
pg3	20-Feb-14	3:16	3:16	0:46	151.58	821.48	Y	2018	CME
pg3	27-Feb-14	16:50	16:50	14:20	158.5	446.57	U	2018	CIR
pg3	25-Mar-14	20:03	20:10	17:40	176.16	449.69	Y	2018	CIR
pg3	19-Apr-14	18:35	18:40	16:10	133.9	432.68	N	2018	CME

To determine whether or not the shock had associated waves, a visual analysis was performed on the time series. As can be seen in the time series below in figure 21, no waves were observed on January 18th, 2016 while periodic waves were observed in figure 22 on June 14th, 2016. There are several problems with using visual analysis to determine the existence of waves however. To start with, the definition of what constitutes a wave is subjective. This can be seen in the time series in figure 21 for January 18th, 2016 below in which it could be argued that several of the fluctuations around 22:20 could be counted as small amplitude waves with short periods. For my research I chose to ignore these and not count them as waves because examples like this do not always show a significant number of repetitions like that of June 14th, 2016 in figure 22. In addition, their small amplitude means they could be hidden in larger trends of the data. While

the initial detrending of the data was performed to make this type of analysis easier, data detrending is not perfect and only eliminates overall trends in the data while leaving local variations capable of hiding small amplitude waves.

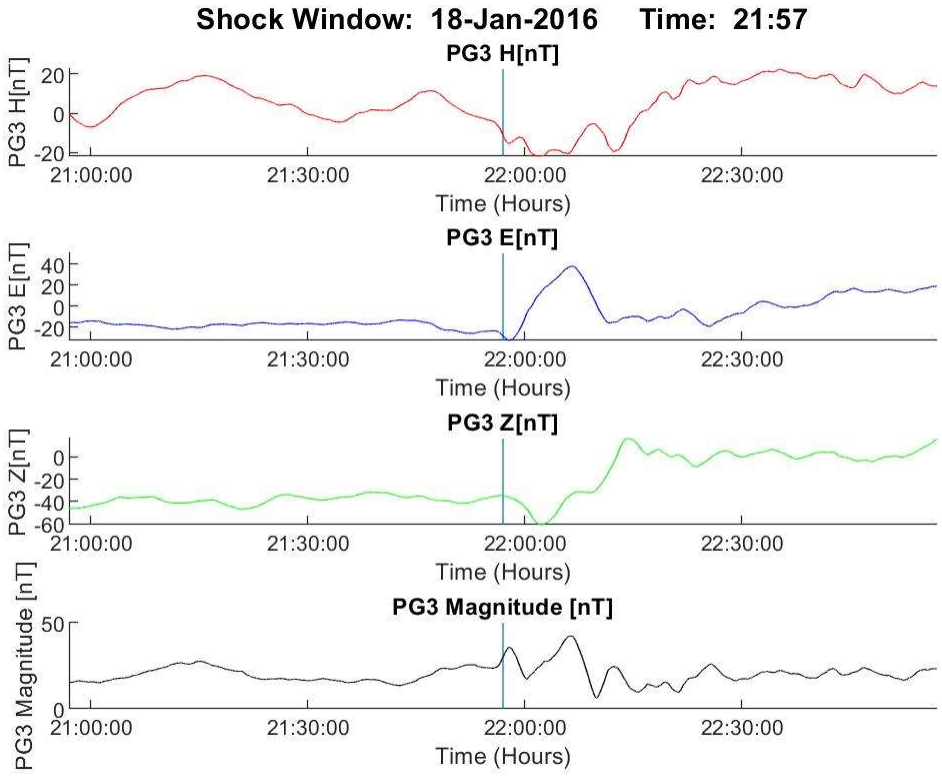

Figure 21:Example PG3 magnetometer data showing a shock with no waves. H[nT] (top), E[nT] (second from top), Z[nT] (third from top), Magnitude (bottom). The vertical blue line marks the shock time given by the Oliveira 2018 shock database.

Figure 21 above provides an example of what a time series without waves looks like in comparison to figure 22 below which clearly shows periodic waves in the H[nT], E[nT], Z[nT], and Magnitude plots with a period of approximately 10 minutes. Additionally, in all the panels except Z[nT], there is a clear drop or increase at the vertical blue line indicating a shock.

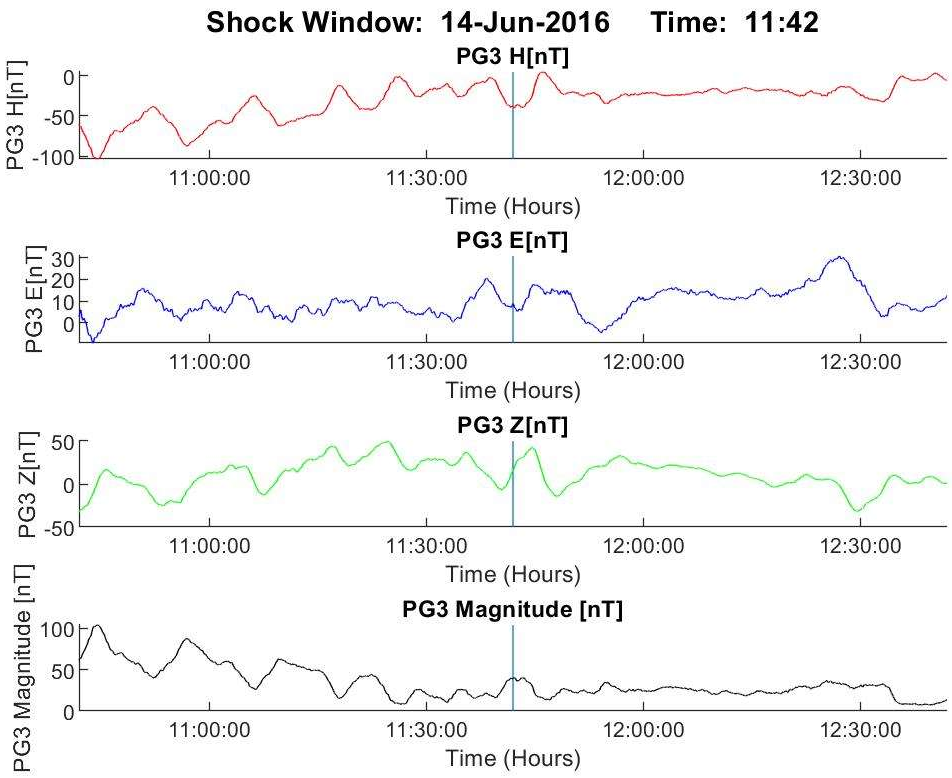

Figure 22: Example PG3 magnetometer data showing a shock with waves. H[nT] (top), E[nT] (second from top), Z[nT] (third from top), Magnitude (bottom). The vertical blue line marks the shock time given by the Oliveira 2018 shock database.

While the shock was easy to see in figure 21, it was more difficult to detect in figure 22. The actual signature of the shock itself is substantially smaller than the periodic waves.

The events in the full excel file described in table 1 were divided into categories based on whether they were inclined shocks or frontal shocks using the same angle ranges given in the histogram plots that will be discussed later (i.e. Inclined shocks have impact angles from 90 degrees to 135 degrees while frontal shocks have angles from 135 degrees to 180 degrees). For both of these categories, the number of waves were counted. In the table above the existence of waves was specified with a *Y* signifying the existence of waves, an *N* signifying a lack of waves, and a *U* signifying that the existence of waves was unknown. The occurrence rate of waves was then defined by the following equation.

$$\frac{(\#\ of\ Y)}{(\#of\ events, or\ U+N+Y)} \qquad (7)$$

The results of this calculation are reported in the results section below. The last category *U* was created due to the aforementioned difficulties with determining what is counted as a wave and what it not. It is recommended that future research utilize a method other or in addition to a visual analysis to determine the existence of waves.

Determining the cause of the shocks was more difficult. The Oliveira shock list does not distinguish between shocks caused by CME's, those caused by CIR's, and those caused by other events. As a result, to make this determination, the Oliveira database was compared to several online databases, notably those maintained by Caltech and Harvard [31], [32] which list CME's in the case of Caltech and shocks detected by various spacecraft in the case of Harvard. Finding a list of CIR's was more difficult, and as a result, CIR's were determined by looking for their characteristic signatures in the Harvard database (a slow solar wind then a large pressure increase followed by a high-speed solar wind lasting days/weeks).

In summary, the example IP shock on 18 January 2016 was used to describe the steps used to calculate the power spectral density and percent difference. The steps used are outlined below.

1. The shock time was used to determine the hour-long shock windows before and after the shock excluding the five minutes around the shock. The shock time is shown as a vertical blue line for an example shock event on 18 January 2016 in figure 17.
2. Welch's method was used to obtain the power spectral density for the H[nT] component for both the "before" and "after" windows. The H[nT] component is shown in the top panel of Figure 17, and the resulting before and after power spectra for that event are shown as a blue and orange line in Figure 20, top.
3. The percent difference was calculated using equation 6. The result for the 18 January 2016 event is shown in the bottom of Figure 20.

These percent differences can then be used to test the hypothesis. This can be done by examining the percent difference plots (the bottom panel of Figure 20 in our example). In Figure 20, we can see that at frequencies greater than 3 mHz, the percent difference in the Pc5 range fluctuates between 2 and 3 on the log10 scale. This means that in reality, the percent difference between the power spectra before and after the shock fluctuates between 100% and 1000%. As 3 mHz and 7 mHz have periods of ~ 5 minutes and ~ 2 minutes respectively, we can see wave activity in this frequency range in the top panel of Figure 17. While this wave activity can be seen before the shock, it dramatically increases after the shock. As past studies have found that IP shocks excite Pc5 wave activity with comparable amplitudes (Kim et al., 2015), this observation is not unusual for either inclined or frontal shocks [33].

Chapter 3

Results: Statistical Analysis to Test Hypothesis

While the power spectra of each individual shock provides useful information about its properties, the goal of the research was to determine if the impact angle of the interplanetary shock affects the occurrence rate of Pc5 waves. This requires a change from the preceding analysis which looked at individual shock characteristics, to an analysis focused on the characteristics of the group of shocks as a whole. To accomplish this, a histogram showing the occurrence rate of different percent differences was made using the information from the percent difference plots described above. The percent difference at a specific frequency was taken and plotted in a histogram to show the distribution of these percentages at different frequencies. It should be noted that these percent differences are on a log10 scale and would need to be converted by raising 10 to the power of the percent difference in question to convert to the actual integer valued percent difference. For example, to find the actual percent difference of 2.5, 10 should be raised to the power of 2.5. This converts the log10 scaled percent difference of 2.5 to a real percent difference of 316.2.

In the below histograms, the top panel displays the resulting histogram if the occurrence rates of the various percent differences were taken at a given frequency. The middle panel shows the distribution of the percent differences of the inclined shocks (defined as having an impact angle between 90 degrees and 135 degrees), while the bottom panel shows the distribution of the percent differences of the frontal shocks (defined as having an impact angle between 135 degrees and 180 degrees).

In the histograms below, only shocks measured at PG3 were used as this removed any effects due to the different latitudes of the magnetometers. Figures 23, 24, and 25 show the occurrence rates at 2 mHz, 3 mHz, and 6 mHz respectively. These were chosen as they provide a decent spread of the Pc5 range. Histograms of the remaining frequencies in the Pc5 range can be found in the appendix. It should also be noted that there is a clear distinction between the occurrence rates of the inclined shocks and those of the frontal shocks.

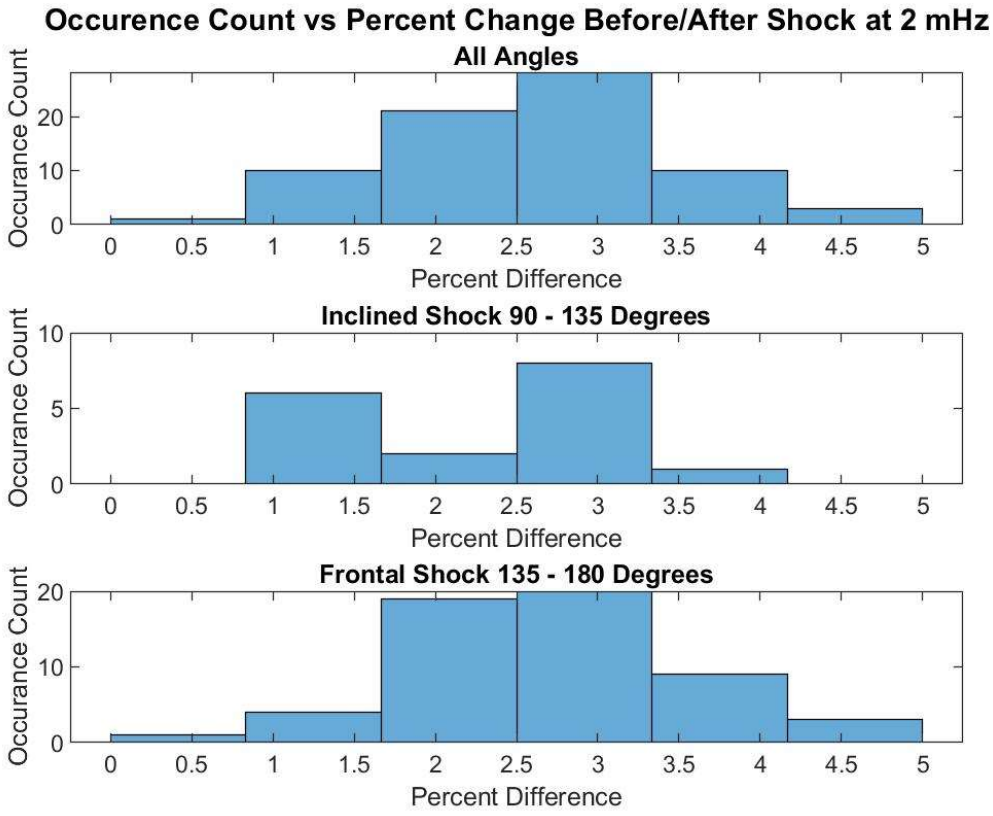

Figure 23: Occurrence Count vs Percent Change Before/After the Shock at 2 mHz. The top panel shows the occurrence count for all the shocks, the middle panel shows the occurrence rate for the inclined shocks, and the bottom panel shows the occurrence rate for the frontal shocks.

As is clearly seen in the top panel in figure 23, the percent differences follow a roughly gaussian curve with the majority of them falling somewhere around a median percent difference of 2.6 (real value 398.1). When this is broken down between the frontal shocks and the inclined shocks, it becomes apparent that not only are frontal shocks much more common than inclined shocks (this will be discussed later), but that at 2 mHz, the frontal shocks still maintain a roughly gaussian distribution, although the most populous bin in the histogram is no longer clearly defined and is instead spread almost evenly between two bins, resulting in a median of around 2.5 (316.2). The inclined shocks are where the similarities end. They do not follow the roughly gaussian shape of the frontal shocks. This means that the reason the combined group has a roughly gaussian shape is due to the overwhelming numerical superiority of the frontal shock group in comparison to the inclined shock group. In addition, while we were able to roughly estimate a median for the frontal shock group due to the fact that most of the shocks were concentrated around 2.5, we are unable to follow the same approach for the inclined shocks because while we could calculate a median value, it would not accurately reflect what is happening. This is because there are two significant groupings of shocks around 1.2 and 2.9. In reality, these are percent differences of 15.8 and 794.3 respectively. This is a significant difference in power level differences between the groupings. It is also important to note that if one looks at the location of the occurrences of the inclined shocks when superimposed onto the frontal shocks, it becomes evident that while both groups have a significant grouping around 3 (actual 1,000 percent), the general trend of the inclined shocks is towards having lower percent

differences between power levels while the trend of the frontal shocks is towards having larger percentage differences.

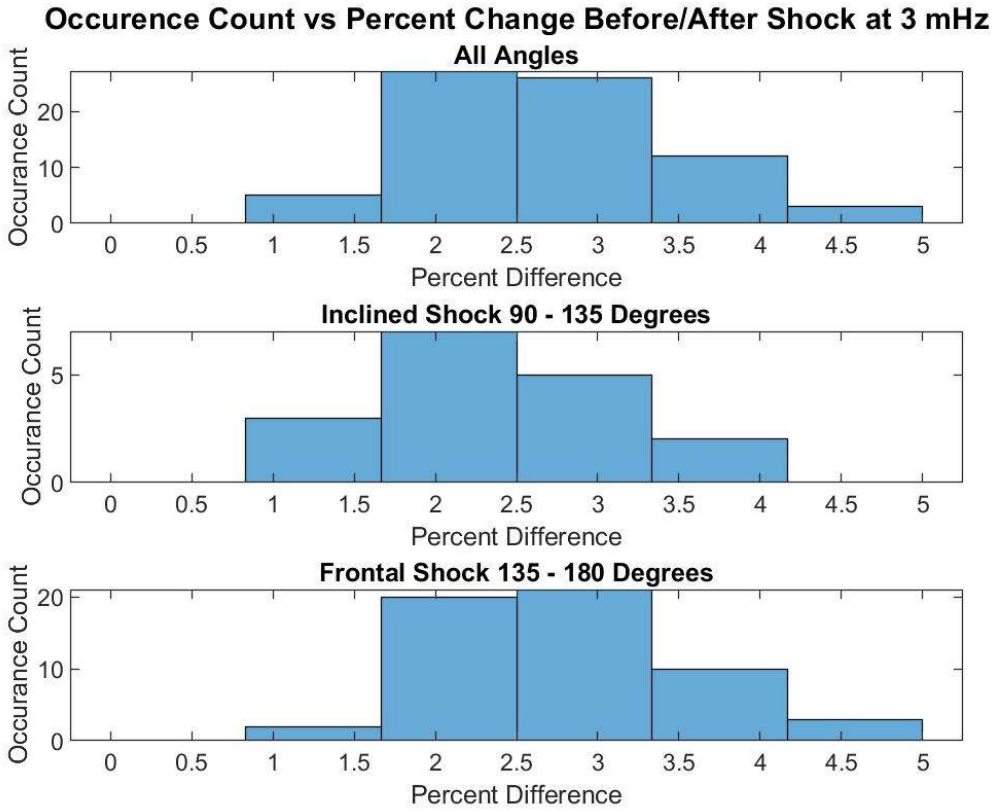

Figure 24: Occurrence Count vs Percent Change Before/After the Shock at 3 mHz. The top panel shows the occurrence count for all the shocks, the middle panel shows the occurrence rate for the inclined shocks, and the bottom panel shows the occurrence rate for the frontal shocks.

In contrast to the histograms at 2 mHz in figure 23, the histograms at 3 mHz in figure 24 show a somewhat different trend, although they do share some of the same characteristics. Overall, we can still see the same roughly gaussian shape as before with a median around 2.6 (actual 398.1 percent), however this time it should be noted that the tails are shorter as most of the percent differences occur in a narrower range of values. We can still see however that the frontal shocks are more gaussian in nature as they have a wider spread of percent differences than the inclined shocks. Like the histogram at 2 mHz, there is a large cluster in the frontal shocks around 2.5 but the percent differences are shifted more towards the higher end of the range leading to a median of about 2.8 (actual 631 percent). Interestingly, unlike the inclined shocks at 2 mHz, the inclined shocks at 3 mHz follow a roughly gaussian trend like the frontal shocks. While they are more gaussian than at 2 mHz, they similarly follow the trend of being numerically fewer with a preference towards having percent differences in the lower region of the histogram. It is also interesting to note that in comparison to 2 mHz, the overall percent differences are higher at 3 mHz with a median around 2.8 (actual 631 percent). There is also a frontal shock trend at both 2 mHz and 3 mHz where there is a more defined jump in occurrence rates of smaller percent differences than there is at higher percent differences.

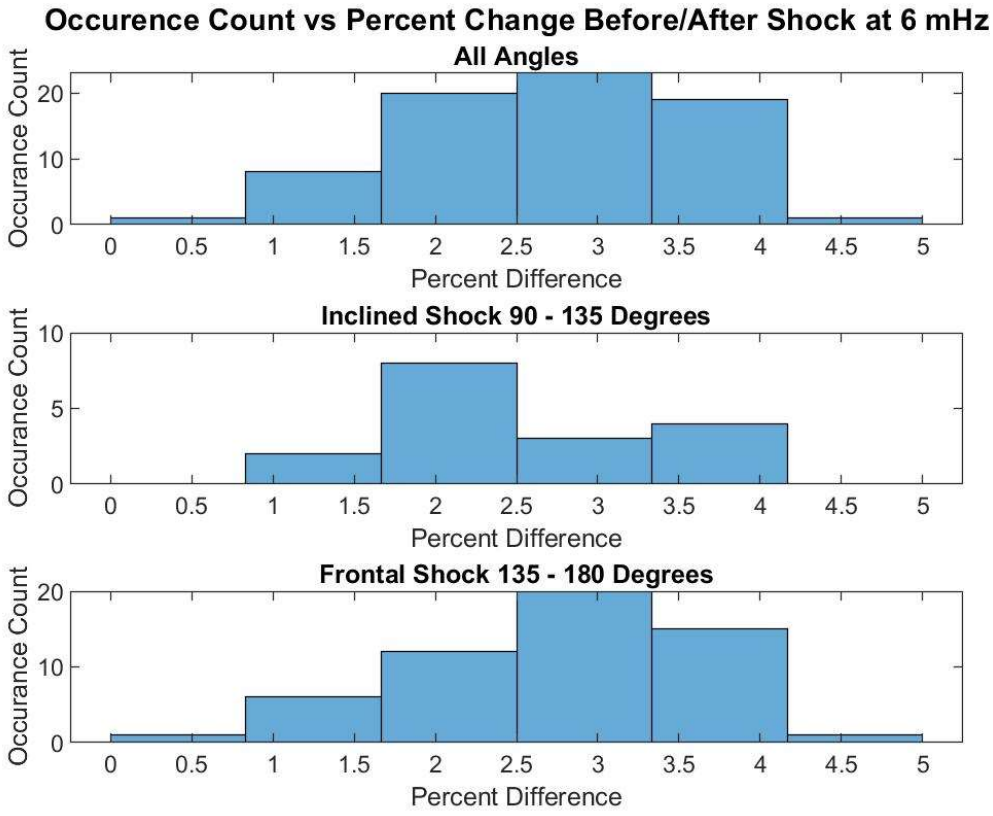

Figure 25: Occurrence Count vs Percent Change Before/After the Shock at 6 mHz. The top panel shows the occurrence count for all the shocks, the middle panel shows the occurrence rate for the inclined shocks, and the bottom panel shows the occurrence rate for the frontal shocks.

In contrast to figures 23 and 24 above showing the histograms at 2 mHz and 3 mHz respectively, the histograms shown in figure 25 are different as they take look at a different part of the Pc5 range. The difference between 2 mHz and 3 mHz is 1 mHz and both of them are located in the lower-mid section of the Pc5 range. In contrast, the difference between 3 mHz and 6 mHz is 3 mHz and 6 mHz is located towards the upper end of the Pc5 range. While like at 2 mHz and 3 mHz in figures 23 and 24 above, there is a general gaussian shape to the data. In this case, the data overall is very centralized with distinct drops in occurrence rates towards the tails. Like 2 mHz in figure 23, the frontal shocks are the much more gaussian of the two groups and tend to skew more towards the upper end of the histogram. By contrast however, unlike at 2 mHz where most of the frontal shocks were concentrated in two bins, the frontal shocks at 6 mHz are more spread out over multiple bins but still concentrating around 2.8 (actual 631 percent). Interestingly, in a similar manner as at 2 mHz, the inclined shocks do not follow a gaussian shape, but instead concentrate at specific percent differences. Unlike at 2 mHz however where there were two predominate bins, the inclined shocks at 6 mHz have a single predominant bin at 2 (actual 100 percent) with the rest of the shocks spread out in the surrounding bins at roughly equal rates. It is interesting to note that at all of the frequencies we have examined, the overall median percent difference was around 2.9 (actual 794.3 percent).

Finally, our visual inspection analysis can provide a complementary test of the hypothesis that shock impact angle affects wave properties. By analyzing the excel spreadsheet, it was found that

the occurrence rate of waves varied significantly depending on whether or not the interplanetary shock impact was inclined or frontal. For the inclined shocks detected by PG3, it was determined that out of 16 detected shocks, 7 of them produced waves. This gave an occurrence rate of 43.75%. For the frontal shocks detected by PG3, it was determined that out of 56 detected shocks, 21 of them produced waves. This gave an occurrence rate of 37.5%. Not only does this show that frontal shocks are much more common, with 3.5 times more frontal shocks than inclined shocks, but that the percentage that produce waves is lower than that of the inclined shocks. This supports the assertion that shock impact angle affects Pc5 wave activity, consistent with power spectral analysis. However, it is harder to reconcile the lower occurrence for inclined shock wave activity found from visual inspection to the higher increase in wave power found from automated power spectral analysis. This may be due to limitations of the visual inspection. As the time series were visually examined to determine whether or not they contained waves and as a result these findings are subjective, it is recommended that future inspection of the time series have a more defined definition or technique for determining if the time series contained waves.

Chapter 4

Discussion

We have tested the question "Does interplanetary shock impact angle affect the occurrence rate of Pc5 waves observed by high-latitude ground magnetometers?" by examining 72 shocks measured by PG3 and have determined that the interplanetary shock impact angle does have a significant effect on the occurrence rate and properties of Pc5 waves, though more events are needed as shown in the table below.

Table 2: Median log10 scaled Percent Difference and 95% Confidence Intervals at Pc5 Frequencies

Frequency	Median Percent Difference, All Shocks 95% Interval	Median Percent Difference, Inclined Shocks 95% Interval	Median Percent Difference, Frontal Shocks 95% Interval
2 mHz	**2.6002** 2.3138-3.0055	**2.7549** 1.9121-3.0030	**2.5831** 2.3182-3.0612
3 mHz	**2.6487** 2.3716-2.9001	**2.1116** 1.8767-2.9486	**2.7975** 2.4975-2.9747
4 mHz	**2.7983** 2.4521-2.9030	**2.1650** 0.8864-2.8245	**2.8216** 2.5614-3.0269
5 mHz	**2.8945** 2.6652-2.9701	**2.4821** 1.8217-3.2169	**2.9193** 2.6661-2.9874
6 mHz	**2.8458** 2.5340-3.2417	**2.4500** 1.9047-3.0218	**2.9309** 2.5567-3.2886
7 mHz	**2.6451** 2.5420-3.0901	**2.0272** 1.8978-2.7523	**2.8577** 2.4780-3.1366

Table 2, the result of a bootstrap analysis, shows the median percent difference of all the shocks, the inclined shocks, and the frontal shocks as well as their respective 95% confidence intervals at several Pc5 frequencies. From the table it is clear that the median percent difference of the inclined shocks is lower than that of the frontal shocks with the exception of 2 mHz, though this exception is due to an apparent bimodal distribution in the percent differences due to the relatively small sample size. While there is an overlap between the 95% confidence intervals of the inclined shocks and the frontal shocks, these differences indicate that the impact angle has an effect on the median percent difference.

Figures 23, 24, and 25 above, showing the Occurrence Count vs Percent Change Before/After the Shock at 2 mHz, 3 mHz, and 6 mHz respectively, all clearly indicate that the impact angle of

the shock has a significant effect on the occurrence rate of Pc5 waves. While on the whole it was found that the occurrence rates of the percent differences produced a roughly gaussian shape, this was very dependent on a combination of the general gaussian nature of frontal shocks as well as their large numerical superiority over inclined shocks. It was also found that frontal shocks tended to have a preference for larger percent differences than inclined shocks.

Inclined shocks on the other hand, appear to have some type of frequency dependence. At frequencies of 1 mHz, 3 mHz, 4 mHz, 5 mHz, and 7 mHz, inclined shocks do show gaussian style distributions, though the shape of their gaussians varies wildly. At frequencies of 2 mHz and 6 mHz, however, the distribution of inclined shocks tends to be more clustered around one or two bins with a scattering among the remaining bins.

While inclined shocks exhibit some form of frequency dependence in their percent difference distributions, they consistently show a preference for smaller percent differences overall than frontal shocks.

Chapter 5

Summary, Implications, and Future Work

5.1 Summary and Implications

Interplanetary (IP) Shocks are capable of having far reaching implications beyond simple scientific curiosity. They are a direct consequence of a variety of solar events including Coronal Mass Ejections and Co-rotating Interaction Regions [1]. Their interaction with the Earth is strong enough that they can shift the bow shock and magnetopause Earthward. They can also pose a danger at the human level by generating electrical currents in technological infrastructure that can overload transformers, communication cables, and power grids. As they pose a danger to our society, understanding them is prudent. A large portion of the current research into their behaviors has been focused on models and simulations and has shown that the shock impact angle should affect the properties of the waves. A significant implication of this study is that it is important to know the impact angle of the shock to predict ground magnetic perturbations and GIC.

The results of this investigation clearly demonstrate that the impact angle of an interplanetary shock has a significant effect on the occurrence rate of Pc5 waves. This is evidenced by figures 23, 24, and 25 above which show clear differences in the distributions of the percent difference in the power spectra caused by the shock between frontal shocks and inclined shocks. Not only do inclined and frontal shocks occur at very different rates, they tend to have very different distributions as well with frontal shocks tending to be more gaussian and shifted towards higher percent differences while inclined shocks may or may not appear gaussian and exhibit some type of frequency dependence in this regard and were generally shifted towards lower percent differences. These results are summarized below.

- Interplanetary Shock impact angle has an effect on the occurrence rate and properties of Pc5 waves.
- Frontal shocks are more common than inclined shocks
- Frontal shocks follow a gaussian distribution of their percent differences
- Frontal shocks have a trend towards larger percent differences while inclined shocks have a trend towards smaller percent differences
- For inclined shocks, the percent change in power appears to vary with frequency

The results of this research are important because they experimentally verify the results of prior theories and simulations in the field. In addition, throughout the course of the investigation, several interesting observations were made in the data, which, while outside of the scope of this investigation, warrant further research to expand our understanding of ULF waves and IP shocks. These will be elaborated upon below in the future work section. In addition, an increased understanding in the generation of magnetic perturbations and their relation to GIC will enable us to better protect ourselves from some of the possible effects mentioned above including shielding or otherwise protecting devices such as high-voltage power transformers and communications cables from Geomagnetically Induced Currents.

We have determined that while the impact angle is a significant factor in the generation of Pc5 waves, the effects of other factors cannot be ignored. This is why the research focused mainly on PG3 instead of including multiple magnetometers. PG3 gave a significant number of events spanning several years while allowing us to ignore other complicating factors such as the effects of variable station latitude, which would likely complicate the analysis by introducing other effects such as latitude dependent ionospheric conductivity and wave frequency.

5.2 Future Work

While the results gained from this research are interesting, there are several paths of continuing research that should be pursued to gain a better understanding of the effects of interplanetary shock impact angles.

Throughout the course of this research, there were many opportunities to explore this topic in a more general sense, however as they were outside the scope of the research, they were ignored. Several of them, however, warrant a closer look and should be investigated further in the future. The most interesting of these are outlined below.

Oliveira and Raeder 2014 discuss how the normals of most CME generated shocks are concentrated near the Sun-Earth line while those driven by CIRs tend to have normals that are inclined with respect to the Sun-Earth line. A future investigation could continue the work begun here in determining the driving force of the shocks and compare their respective shock normals to see if this holds true [4].

While this investigation was limited in scope to examining the impact of shock angle on Pc5 wave generation, it is important to remember that Pc5 waves are just one frequency range of ULF waves. Other frequency ranges should be examined as well to determine their susceptibility to influence due to shock impact angle.

Throughout the course of this research, several anomalies were observed in the data. While these events are rare, their existence is worth investigating as they differ significantly from the general trend observed in most of the power spectra.

The most prominent of these were observations made in the power spectra outside of the Pc5 range. Several prominent examples of this are depicted below. In figure 26 below, the power after the shock is usually higher but there is a point around 25 mHz when the power spectra before the shock dominates. There is also an anomaly around 300 mHz in which the difference in power levels suddenly increases.

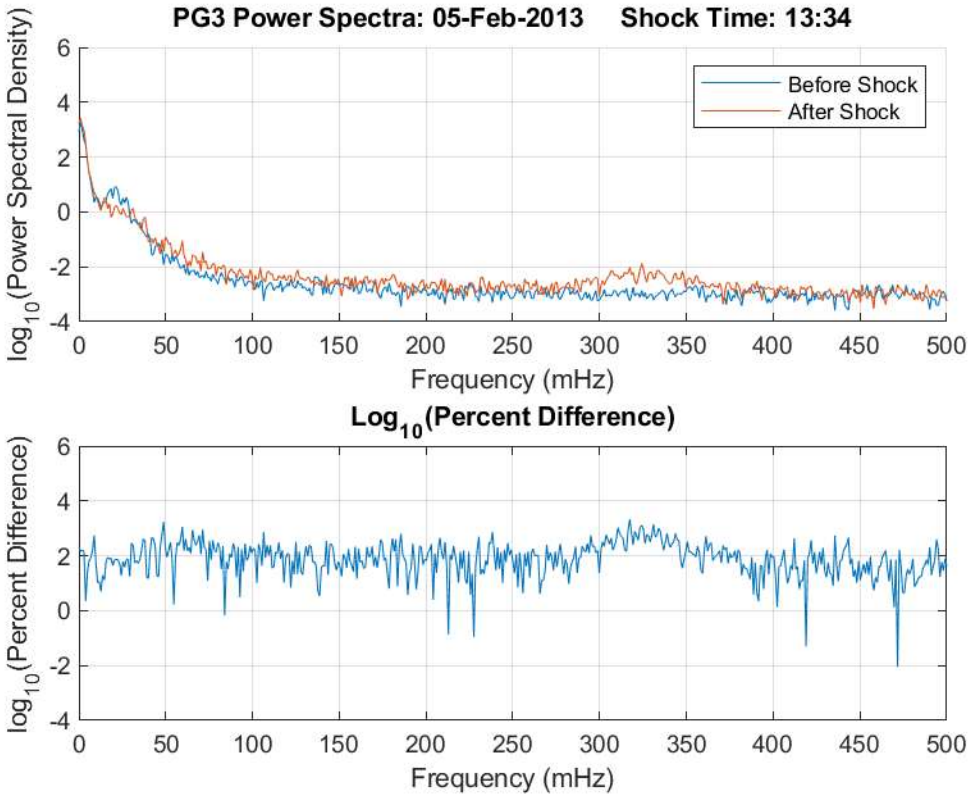

Figure 26: Power Spectra with Event around 300 mHz. The top panel displays the log10 scaled power spectra at various frequencies. The power spectra before the shock is given by the blue line while the power spectra after the shock is given by the orange line. The bottom panel displays the log10 scaled percent difference between the two spectra in the top panel.

Like figure 26 above, figure 27 below contains a region where the percent difference in power levels before and after the shock drastically increases, although this happens at a lower frequency (100 mHz) than in figure 26 above (300 mHz). However, it must also be noted that at around 350 mHz, the power before the shock becomes dominant over that after the shock. While this does not create a significant change in their percent differences, it is unusual regardless. Not only that, but the fact that it occurs in roughly the same range as the increase in percent difference found in figure 26 makes it noteworthy.

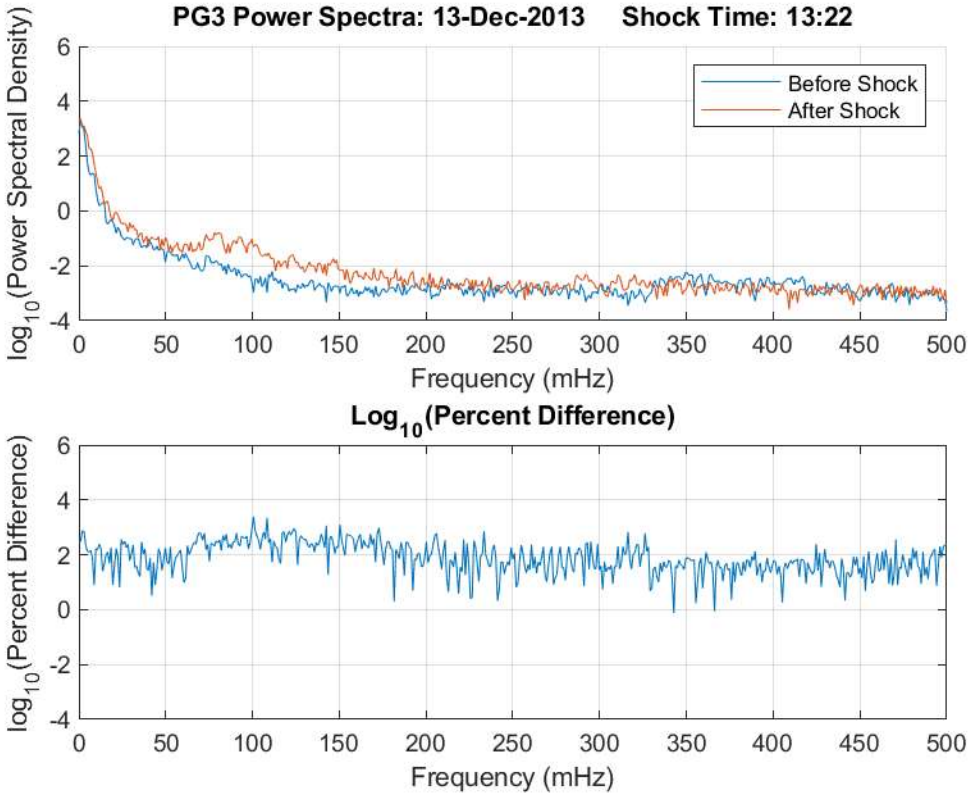

Figure 27: Power Spectra with Interesting Features Outside of the Pc5 Range. The top panel displays the log10 scaled power spectra at various frequencies. The power spectra before the shock is given by the blue line while the power spectra after the shock is given by the orange line. The bottom panel displays the log10 scaled percent difference between the two spectra in the top panel.

While the majority of the results of the power spectra analysis show the power level increasing after the shock, there are several examples like figure 28 below where the power spectra before the shock dominates that after the shock, implying that the shock caused a drop in the power. While this is not the only example of this oddity, examples such as this are in opposition to the general consensus of the results which demonstrate an increase in the power spectra after the shock impact.

Additionally, the power spectra in figure 28 displays some form of periodicity. This is especially apparent in the power spectra before the shock but can be seen after the shock as well. This is highly unusual as is illustrated by the other power spectra shown in this paper. The variation in the percent difference is also highly abnormal and is generally maintained at the same level.

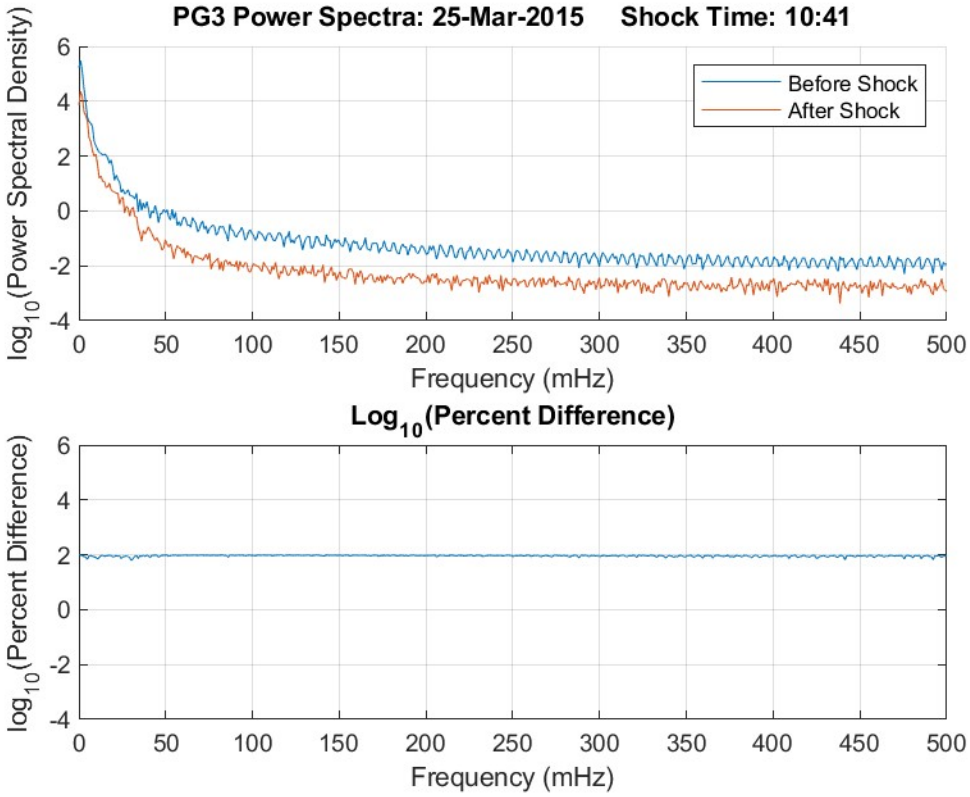

Figure 28: Power Spectra with Larger Power Level Before the Shock than After. The top panel displays the log10 scaled power spectra at various frequencies. The power spectra before the shock is given by the blue line while the power spectra after the shock is given by the orange line. The bottom panel displays the log10 scaled percent difference between the two spectra in the top panel.

Another avenue for future research would be to include more of the magnetometers in order to determine if there is a latitude dependence on the observed power spectra from the shocks, as well as taking the time of day of the shocks into account as this could effectively change the location of the magnetometers to the dark side of the Earth in the Earth-Sun system.

For this investigation the shocks were broken up into two predominant groups based on their impact angle, inclined shocks with angles between 90 degrees and 135 degrees, and frontal shocks with angles between 135 degrees and 180 degrees. For the inclined shocks, no distinction was made regarding whether the shocks were inclined northward or southward. It is recommended that any future analysis of this type should either take this into account from the beginning or divide the inclined shocks into sub categories based on this factor. While it is theorized that part of the non-gaussian nature and preference for separated bins of the inclined shocks is due to the north/south orientation of the inclination, further research must be conducted to determine if this is in fact the case.

During the course of this investigation, a different and or sub hypothesis began to take form concerning whether inclined shocks generate different frequencies than frontal shocks. In other words, “Does the shock impact angle affect the frequency of ULF waves?” If this is the case,

different frequencies could be excited across the ULF spectrum based on the shock impact angle leading to a type of frequency “signature” for different angles.

Appendix A

Figures 29, 30, and 31 show the Pc5 histograms not included in the main body of the text above.

In figure 29, the inclined shocks follow a gaussian distribution like the frontal shocks. However, as was mentioned above, the distributions of these percent differences tend to be lower than those of the frontal shocks. This pattern was repeated in figures 30 and 31.

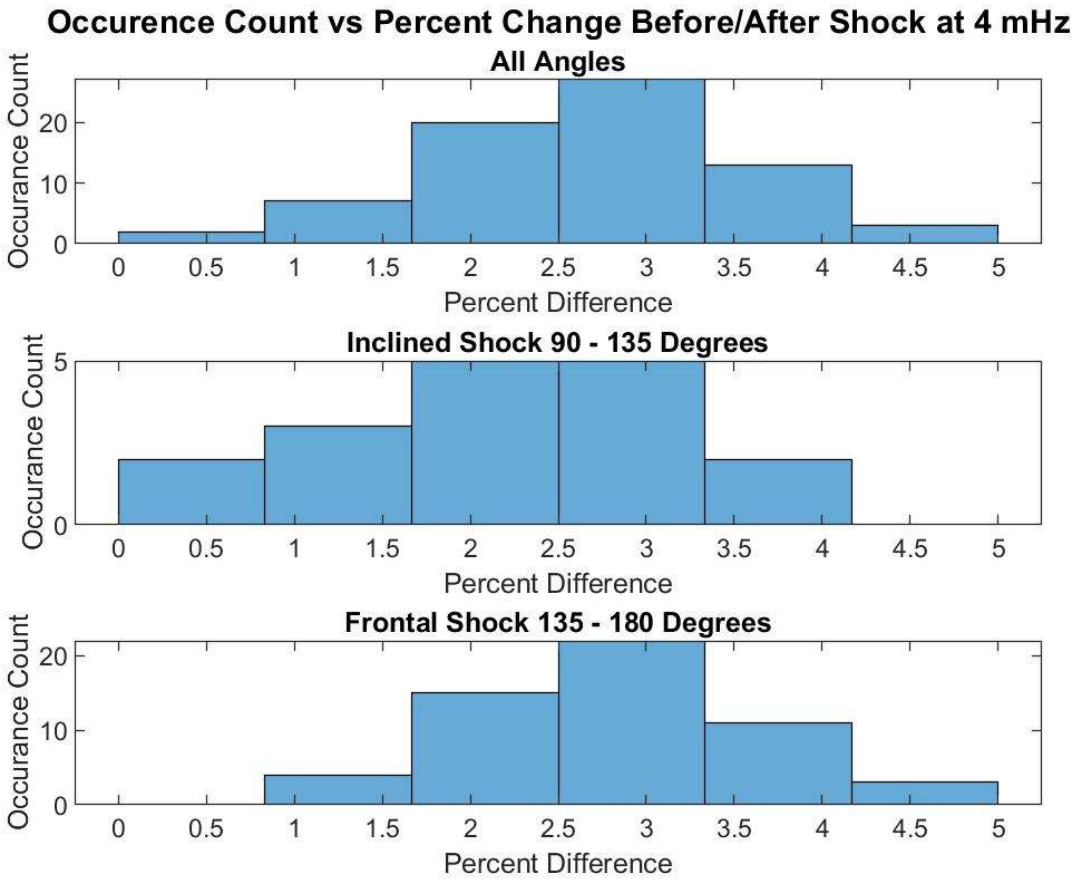

Figure 29: Occurrence Count vs Percent Change Before/After the Shock at 4 mHz. The top panel shows the occurrence count for all the shocks, the middle panel shows the occurrence rate for the inclined shocks, and the bottom panel shows the occurrence rate for the frontal shocks.

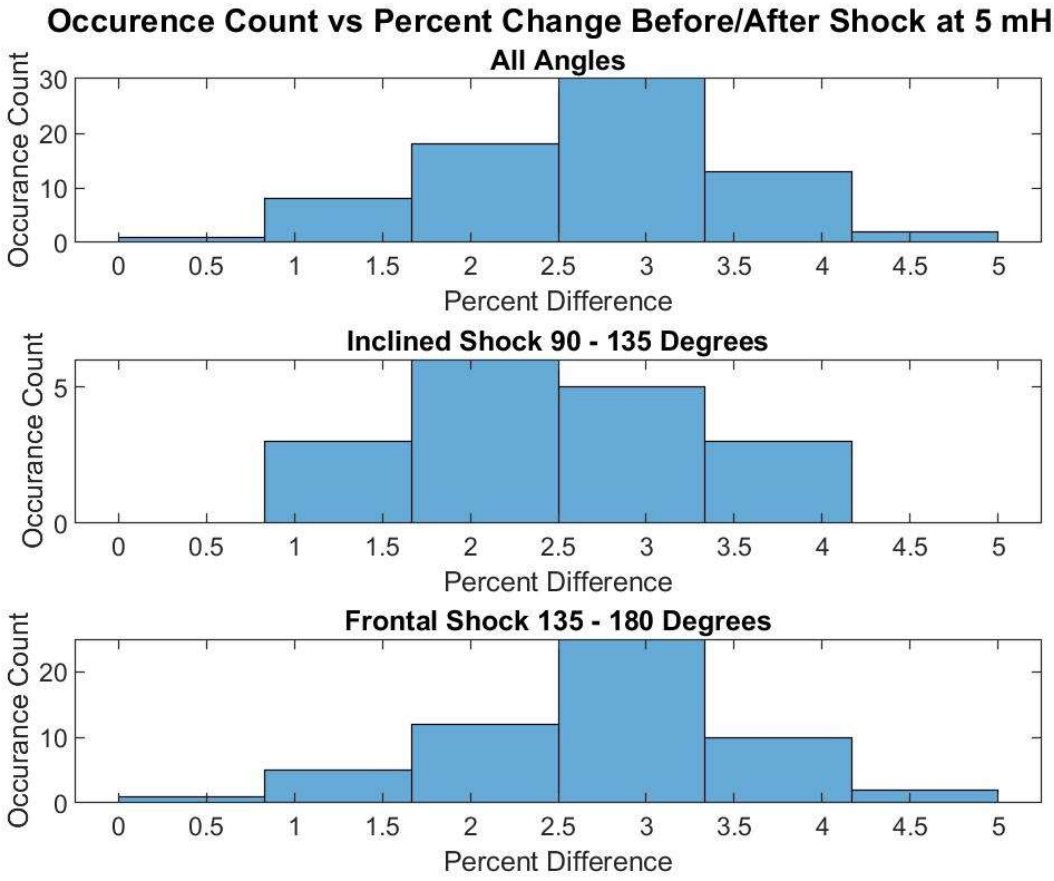

Figure 30: Occurrence Count vs Percent Change Before/After the Shock at 5 mHz. The top panel shows the occurrence count for all the shocks, the middle panel shows the occurrence rate for the inclined shocks, and the bottom panel shows the occurrence rate for the frontal shocks.

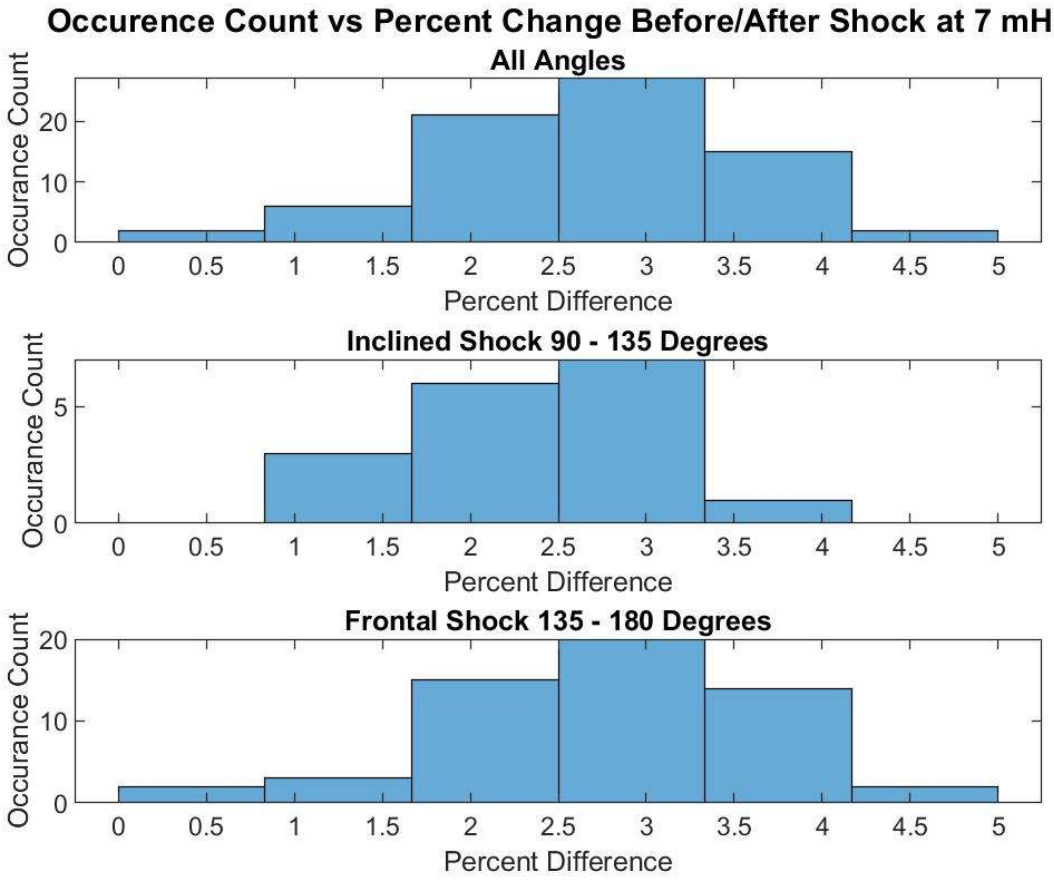

Figure 31: Occurrence Count vs Percent Change Before/After the Shock at 7 mHz. The top panel shows the occurrence count for all the shocks, the middle panel shows the occurrence rate for the inclined shocks, and the bottom panel shows the occurrence rate for the frontal shocks.

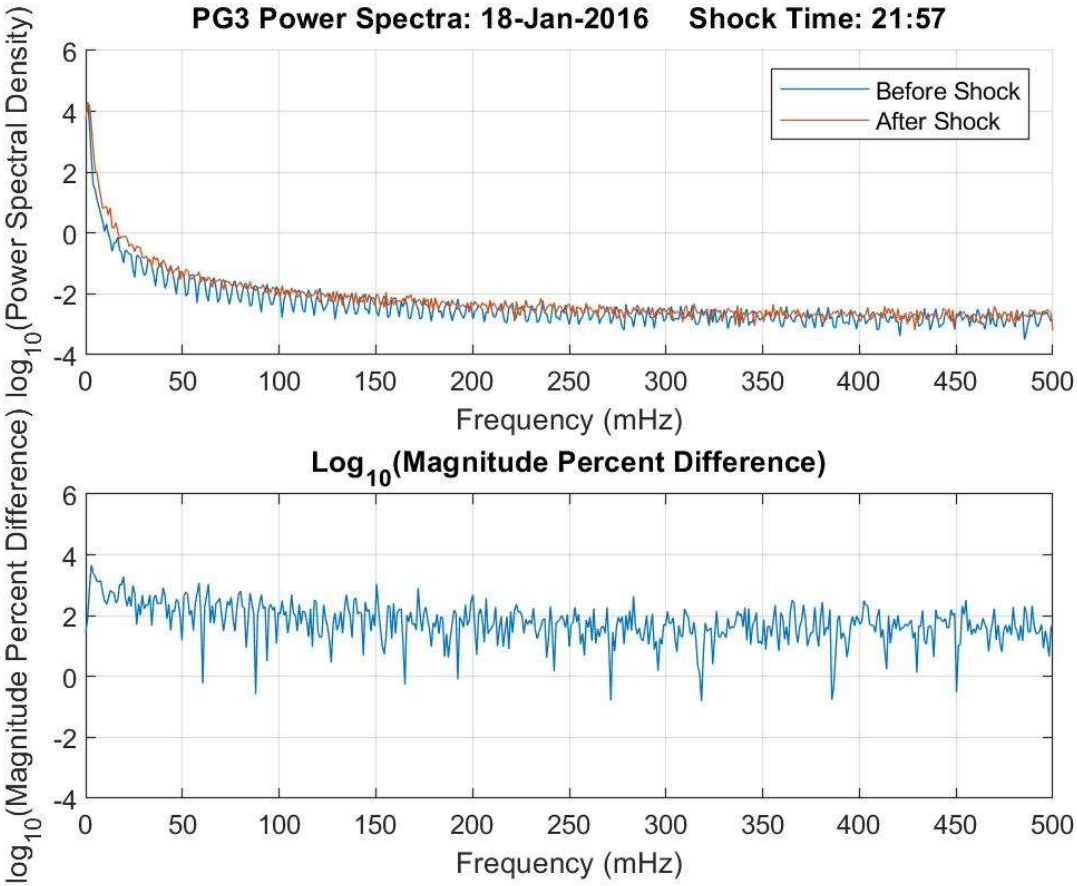

Figure 32: PG3 Magnitude Power Spectra for January 18th, 2016. The top panel displays the log10 scaled power spectra at various frequencies. The power spectra before the shock is given by the blue line while the power spectra after the shock is given by the orange line. The bottom panel displays the log10 scaled percent difference between the two spectra in the top panel.

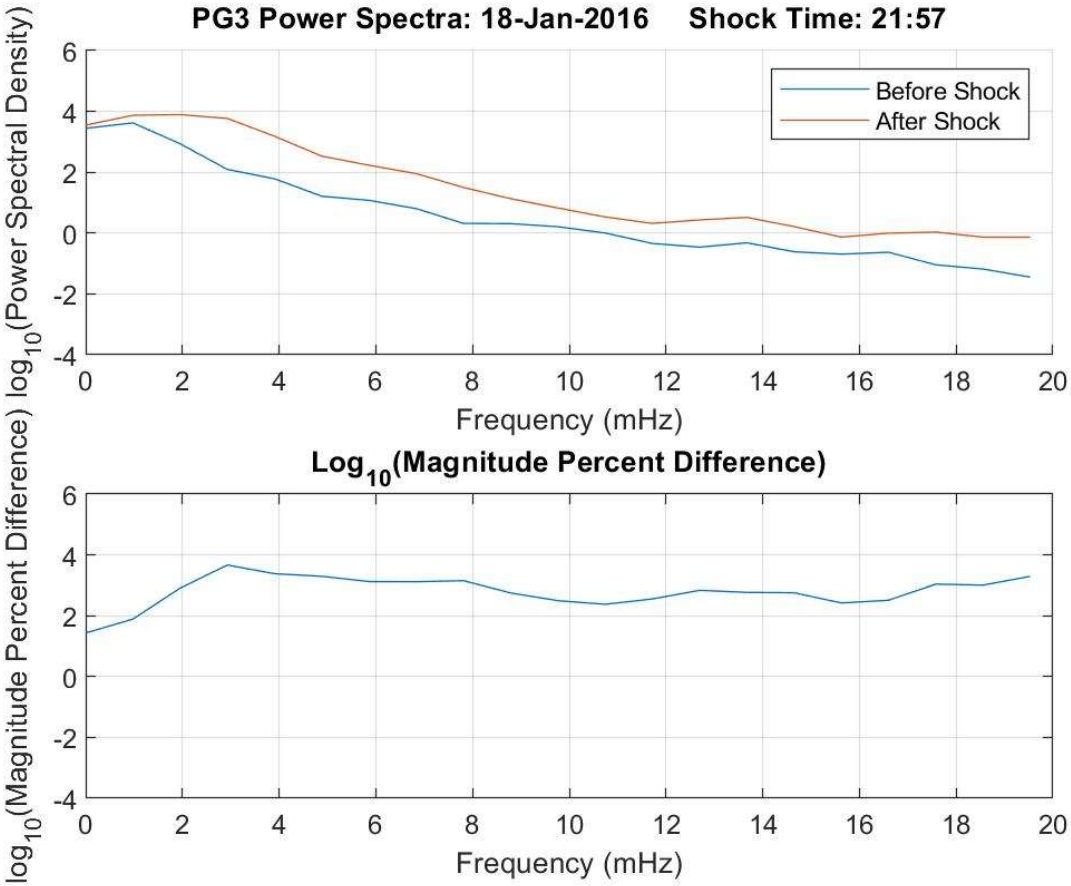

Figure 33: PG3 Magnitude Power Spectra for January 18th, 2016. The top panel displays the log10 scaled power spectra at various frequencies. The power spectra before the shock is given by the blue line while the power spectra after the shock is given by the orange line. The bottom panel displays the log10 scaled percent difference between the two spectra in the top panel.

Figures 32 and 33 above show the same type of power spectrum analysis performed in the main body of the text above, however instead of performing the analysis on H[nT], the analysis was performed on the Magnitude. Both H[nT] and the Magnitude show an increase in the power spectra after the shock, and while they are vey similar, the Percent Differences for the Magnitude plots are slightly higher than those of the H[nT] plots.

Table 3: Interplanetary Shock Information (Ground Station, Date, Shock Time, Observed Shock Time, Local Time, Impact Angle, Velocity, and Waves). Waves are labeled as yes "Y", no "N", and unknown "U". The # and #VALUE! In the Observed Shock Time and Local Time indicate a lack of data fot the shock in qustion.

Ground Station	Date	Shock Time	Observed Shock Time	Local Time (UTC - 2.5)	Angle (degrees)	Velocity (km/s)	Waves (Y/N/U)
pg3	17-Jan-13	0:10	0:10	0:10	150.99	398.72	N
pg3	19-Jan-13	17:33	17:40	17:40	127.62	345.8	N
pg3	5-Feb-13	13:34	13:40	13:40	131.71	339.73	N
pg3	13-Feb-13	1:30	1:35	1:35	112.24	211.64	Y
pg3	16-Feb-13	12:09	12:09	12:09	170.34	441.67	Y
pg3	15-Mar-13	5:26	5:30	5:30	134.33	414.9	Y
pg3	17-Mar-13	5:59	6:00	6:00	172.88	766.4	N
pg3	13-Apr-13	22:52	22:52	22:52	135.2	452.86	N
pg3	23-Apr-13	4:51	4:51	4:51	160.66	301.26	Y
pg3	30-Apr-13	9:49	9:50	9:50	162.08	436.06	N
pg3	18-May-13	1:10	1:10	1:10	170.48	494.98	N
pg3	19-May-13	23:08	23:12	23:12	135.92	423.79	N
pg3	24-May-13	18:10	18:15	18:15	142.79	561.01	N
pg3	25-May-13	9:47	########	#VALUE!	134.96	555.22	U
pg3	29-Oct-13	10:32	10:32	10:32	147.73	385.93	N
pg3	30-Nov-13	20:50	20:50	20:50	163.63	559.14	N
pg3	13-Dec-13	13:22	13:25	13:25	146.09	310.57	N
pg3	7-Jan-14	15:11	15:15	15:15	121.99	297.12	U
pg3	9-Jan-14	20:07	20:10	20:10	135.62	479.41	N
pg3	7-Feb-14	17:06	17:06	17:06	167.75	470.64	Y
pg3	13-Feb-14	9:44	9:45	9:45	157.75	427.56	Y
pg3	15-Feb-14	13:16	13:16	13:16	146.51	475.53	U
pg3	18-Feb-14	6:39	6:40	6:40	141.21	374.15	N
pg3	19-Feb-14	3:47	3:47	3:47	160.08	582.7	N
pg3	20-Feb-14	3:16	3:16	3:16	151.58	821.48	Y
pg3	27-Feb-14	16:50	16:50	16:50	158.5	446.57	U
pg3	25-Mar-14	20:03	20:10	20:10	176.16	449.69	N
pg3	19-Apr-14	18:35	18:40	18:40	133.9	432.68	Y
pg3	20-Apr-14	10:55	10:55	10:55	153.65	373.78	Y
pg3	3-May-14	17:45	17:50	17:50	131.71	309.69	Y
pg3	7-May-14	22:27	22:30	22:30	151.44	331.28	N
pg3	29-May-14	9:29	9:30	9:30	132.25	330.9	N
pg3	7-Jun-14	16:51	16:51	16:51	170.75	461.68	Y
pg3	23-Jun-14	23:07	23:10	23:10	153.41	356.03	Y
pg3	23-Dec-14	11:15	11:15	11:15	161.36	683.43	N
pg3	6-Jan-15	4:08	4:08	4:08	145.58	478.39	N
pg3	7-Jan-15	6:14	6:15	6:15	159.22	494.12	Y
pg3	26-Jan-15	8:33	8:33	8:33	126.42	304.43	N
pg3	11-Mar-15	5:12	5:15	5:15	159.96	425.13	N

pg3	17-Mar-15	4:45	4:45	4:45	172.79	572.19	Y
pg3	21-Mar-15	20:51	20:51	20:51	139.46	622.87	Y
pg3	25-Mar-15	10:41	10:41	10:41	167.91	407.35	Y
pg3	25-Mar-15	19:43	19:43	19:43	168.99	559.31	Y
pg3	31-Mar-15	8:32	8:35	8:35	156.85	405.53	Y
pg3	9-Apr-15	2:13	2:13	2:13	177.38	401.31	N
pg3	9-Apr-15	10:08	10:10	10:10	148.95	358.19	N
pg3	16-Apr-15	5:36	5:36	5:36	153.17	353.72	N
pg3	24-Apr-15	18:17	18:17	18:17	137.54	348.95	Y
pg3	1-May-15	15:29	15:30	15:30	175.67	506.37	Y
pg3	6-May-15	1:41	1:45	1:45	176.93	529.07	N
pg3	13-May-15	9:57	9:57	9:57	153.17	303.7	Y
pg3	5-Jun-15	9:38	9:40	9:40	132.75	241.09	Y
pg3	12-Jun-15	13:04	13:15	13:15	128.32	348.17	Y
pg3	21-Jun-15	16:43	16:45	16:45	140.87	580.29	N
pg3	22-Jun-15	18:33	18:35	18:35	173.72	800.81	N
pg3	24-Jun-15	13:25	########	#VALUE!	126.86	621.98	U
pg3	24-Oct-15	18:54	18:54	18:54	130.46	300.12	N
pg3	4-Nov-15	3:52	3:55	3:55	128.31	510.65	Y
pg3	6-Nov-15	18:19	18:20	18:20	171.49	747.94	U
pg3	18-Nov-15	20:12	20:15	20:15	171.49	496.23	N
pg3	14-Dec-15	13:17	13:20	13:20	150.34	432.4	Y
pg3	19-Dec-15	16:17	16:20	16:20	177.43	563.53	N
pg3	31-Dec-15	0:48	0:50	0:50	135.13	404.17	N
pg3	7-Jan-16	14:50	14:50	14:50	152.78	491.8	Y
pg3	18-Jan-16	21:57	21:57	21:57	135.58	356.94	N
pg3	11-Mar-16	5:31	5:35	5:35	152.78	362	N
pg3	14-Mar-16	17:14	17:15	17:15	141.26	417.03	Y
pg3	14-Apr-16	7:35	7:35	7:35	163.53	577.15	U
pg3	14-Jun-16	11:42	11:42	11:42	162.17	492.24	Y
pg3	9-Nov-16	6:43	6:45	6:45	166.02	347.23	N
pg3	26-Jan-17	8:16	8:20	8:20	171.89	381.51	N
pg3	27-May-17	15:31	15:40	15:40	128.75	394.57	U
pg5	7-Jan-16	14:50	14:48	14:48	152.78	491.8	Y
pg5	18-Jan-16	21:57	22:00	22:00	135.58	356.94	N
pg5	11-Mar-16	5:31	5:32	5:32	152.78	362	N
pg5	14-Mar-16	17:14	17:15	17:15	141.26	417.03	U
pg5	14-Apr-16	7:35	7:38	7:38	163.53	577.15	Y
pg5	14-Jun-16	11:42	11:45	11:45	162.17	492.24	U
pg5	9-Nov-16	6:43	6:45	6:45	166.02	347.23	N
pg5	26-Jan-17	8:16	8:20	8:20	171.89	381.51	N
pg5	27-May-17	15:31	15:40	15:40	128.75	394.57	U
pg5	1-Jul-17	17:12	17:15	17:15	143.75	401.19	Y

pg5	9-Jul-17	0:11	0:11	0:11	168.23	385.12	N

Bibliography

[1] "Introduction to Interplanetary Shocks." [Online]. Available: https://wind.nasa.gov/mfi/ip_descr.html. [Accessed: 03-Mar-2019].

[2] "Travelling interplanetary shocks and CMEs." [Online]. Available: http://www.physics.usyd.edu.au/~cairns/teaching/lecture11/node5.html. [Accessed: 03-Mar-2019].

[3] "Seasons | COSMOS." [Online]. Available: http://astronomy.swin.edu.au/cosmos/s/seasons. [Accessed: 18-Mar-2019].

[4] D. M. Oliveira and J. Raeder, "Impact angle control of interplanetary shock geoeffectiveness," *J. Geophys. Res. Space Phys.*, vol. 119, no. 10, pp. 8188–8201, Oct. 2014.

[5] "Create-a-Water-Ripple-Effect-in-Adobe-Photoshop-Step-8.jpg (1024×768)." [Online]. Available: https://www.wikihow.com/images/5/5f/Create-a-Water-Ripple-Effect-in-Adobe-Photoshop-Step-8.jpg. [Accessed: 18-Mar-2019].

[6] M. G. Kivelson and C. T. Russell, Eds., *Introduction to space physics*. Cambridge ; New York: Cambridge University Press, 1995.

[7] E. N. Parker, "Dynamics of the Interplanetary Gas and Magnetic Fields.," *Astrophys. J.*, vol. 128, p. 664, Nov. 1958.

[8] "Coronal Mass Ejections | NOAA / NWS Space Weather Prediction Center." [Online]. Available: https://www.swpc.noaa.gov/phenomena/coronal-mass-ejections. [Accessed: 04-Mar-2019].

[9] "Reconnection.gif (550×400)." [Online]. Available: https://upload.wikimedia.org/wikipedia/commons/2/24/Reconnection.gif. [Accessed: 04-Mar-2019].

[10] "NASA's Cosmicopia -- Sun - Solar Activity - Coronal Mass Ejections." [Online]. Available: https://helios.gsfc.nasa.gov/cme.html. [Accessed: 04-Mar-2019].

[11] "NASA/Marshall Solar Physics." [Online]. Available: https://solarscience.msfc.nasa.gov/CMEs.shtml. [Accessed: 04-Mar-2019].

[12] "Scientists unlock the secrets of exploding plasma clouds on the sun," *EurekAlert!* [Online]. Available: http://www.eurekalert.org/pub_releases/2010-11/aps-sut110310.php. [Accessed: 04-Mar-2019].

[13] "NASA's Cosmos." [Online]. Available: https://ase.tufts.edu/cosmos/view_picture.asp?id=125. [Accessed: 04-Mar-2019].

[14] "Co-rotating Interaction Region - AMS Glossary." [Online]. Available: http://glossary.ametsoc.org/wiki/Co-rotating_Interaction_Region. [Accessed: 04-Mar-2019].

[15] B. Heber, T. R. Sanderson, and M. Zhang, "Corotating interaction regions," *Adv. Space Res.*, vol. 23, no. 3, pp. 567–579, Jan. 1999.

[16] "Co-rotating Interaction Regions: interactions between fast and slow streams." [Online]. Available: http://www.physics.usyd.edu.au/~cairns/teaching/lecture11/node4.html. [Accessed: 04-Mar-2019].

[17] J. T. Gosling and V. J. Pizzo, "FORMATION AND EVOLUTION OF COROTATING INTERACTION REGIONS AND THEIR THREE DIMENSIONAL STRUCTURE," *Space Sci. Rev.*, vol. 89, no. 1, pp. 21–52, Apr. 1999.

[18] “Earth’s magnetosphere | NOAA / NWS Space Weather Prediction Center.” [Online]. Available: https://www.swpc.noaa.gov/phenomena/earths-magnetosphere. [Accessed: 03-Mar-2019].
[19] “Earth’s magnetosphere and plasmasheet.” [Online]. Available: http://www.planetary.org/multimedia/space-images/earth/earths-magnetosphere-and-plasmasheet.html. [Accessed: 03-Mar-2019].
[20] “Compression And Rarefaction | Longitudinal Waves | Siyavula.” [Online]. Available: https://www.siyavula.com/read/science/grade-10/longitudinal-waves/09-longitudinal-waves-02. [Accessed: 11-Mar-2019].
[21] “Characteristics of Electromagnetic Wave - Definition, Properties, Wave Propagation.” [Online]. Available: https://byjus.com/physics/characteristics-of-em-waves/. [Accessed: 11-Mar-2019].
[22] “SVS: Alfvén Waves - Basic.” [Online]. Available: https://svs.gsfc.nasa.gov/4560. [Accessed: 08-Apr-2019].
[23] R. L. McPherron, “Magnetic Pulsations: Their Sources and Relation to Solar Wind and Geomagnetic Activity,” *Surv. Geophys.*, vol. 26, no. 5, pp. 545–592, Sep. 2005.
[24] J. A. Jacobs, Y. Kato, S. Matsushita, and V. A. Troitskaya, “Classification of geomagnetic micropulsations,” *J. Geophys. Res.*, vol. 69, no. 1, pp. 180–181, Jan. 1964.
[25] M. A. Chelpanov, O. V. Mager, P. N. Mager, D. Yu. Klimushkin, and O. I. Berngardt, “Properties of frequency distribution of Pc5-range pulsations observed with the Ekaterinburg decameter radar in the nightside ionosphere,” *J. Atmospheric Sol.-Terr. Phys.*, vol. 167, pp. 177–183, Jan. 2018.
[26] “Mathematics of Standing Waves.” [Online]. Available: https://www.physicsclassroom.com/class/waves/Lesson-4/Mathematics-of-Standing-Waves. [Accessed: 11-Mar-2019].
[27] “Magnetosphere.jpg (336×492).” [Online]. Available: https://ccmc.gsfc.nasa.gov/staff/ericc/Magnetosphere.jpg. [Accessed: 11-Mar-2019].
[28] D. M. Oliveira and J. Raeder, “Impact angle control of interplanetary shock geoeffectiveness: A statistical study: GEOEFFECTIVENESS OF IP SHOCKS,” *J. Geophys. Res. Space Phys.*, vol. 120, no. 6, pp. 4313–4323, Jun. 2015.
[29] C. R. Clauer *et al.*, “Autonomous Adaptive Low-Power Instrument Platform (AAL-PIP) for remote high latitude geospace data collection,” *Geosci. Instrum. Methods Data Syst. Discuss.*, vol. 4, no. 1, pp. 271–317, Jun. 2014.
[30] D. M. Oliveira *et al.*, “Geomagnetically Induced Currents Caused by Interplanetary Shocks With Different Impact Angles and Speeds: SHOCK IMPACT ANGLES AND GICS,” *Space Weather*, vol. 16, no. 6, pp. 636–647, Jun. 2018.
[31] “List of Richardson/Cane ICMEs Since January1996.” [Online]. Available: http://www.srl.caltech.edu/ACE/ASC/DATA/level3/icmetable2.htm. [Accessed: 07-Apr-2019].
[32] “CfA Interplanetary Shock Database.” [Online]. Available: https://www.cfa.harvard.edu/shocks/. [Accessed: 07-Apr-2019].
[33] H. Kim *et al.*, “Conjugate observations of traveling convection vortices associated with transient events at the magnetopause,” *J. Geophys. Res. Space Phys.*, vol. 120, no. 3, pp. 2015–2035, Mar. 2015.